



UNIVERSITAT
POLITÈCNICA
DE VALÈNCIA



UNIVERSITAT POLITÈCNICA DE VALÈNCIA

School of Design Engineering

Clean seed method for flow visualization in transpiration
cooling

Master's Thesis

Master's Degree in Aeronautical Engineering

AUTHOR: Soriano Lluch, Javier

Tutor: Galindo Lucas, José

ACADEMIC YEAR: 2021/2022

Abstract

Using flow visualization methods such as PIV, LDA,..., is not advisable when interacting with porous materials. The build-up of residue due to the use of particles of this techniques can clog the pores of the structure, rendering the results invalid. The use of carbon dioxide as a seeder is studied. Using an infrared camera and a narrow-band filter at $4.3 \mu m$, the film layer coverage of the coolant can be visualized.

Key Words: IR, flow visualization, transpiration cooling, 3D metal printed porous structures

Abstracto

El uso de algunos métodos de visualización de flujo como PIV, LDA, ..., es desaconsejable en materiales porosos. La acumulación de residuos derivados de las partículas usadas para este tipo de técnicas puede restringir el flujo que pasa a través de estas. En este documento, se estudia el uso del dióxido de carbono como marcador. Mediante el uso de una cámara infrarroja y filtro a $4.3 \mu m$, se obtiene una visualización clara del estado de la película protectora del refrigerante.

Palabras Clave: visualización flujo, IR, refrigeración por transpiración, estructuras porosas impresas en metal

Abstracte

L'ús de mètodes de visualització de flux com ara PIV, LDA,..., no és aconsellable a l'hora d'interaccionar amb materials porosos. L'acumulació de residus per l'ús de partícules d'aquestes tècniques pot obstruir els porus de l'estructura, invalidant els resultats. L'ús del diòxid de carboni s'estudia com a marcador infrarroig és estudiat. Utilitzant una càmera infraroja i un filtre de banda estreta a $4,3 \mu m$, es pot visualitzar la cobertura de la capa de pel·lícula del refrigerant.

Paraules Clau: visualització del flux, IR, refrigeració per transpiració, estructures poroses impreses en metal

Acknowledgments

First of all, I would like to express my gratitude to Dr. Ir. M. Kinell and Dr. Ir. A. Bonaldo for giving me the opportunity to perform my thesis at Siemens Energy and helping me through all the process. I would also like to thank Daniel Roman for his help while designing and building the test rig. It is not a stretch to say that without him I would have had to sand a lot of plastic because of “not so easy to spot mistakes”.

Special thanks also to my colleagues in the Fluid Dynamics Lab. The countless hours spent together were just incredible. I know that none of us will never forget Zack, memories like that are just..., they there to stay and laugh every time you think about them.

About my family, what can I say. I will not have been possible to accomplish what I have done without them. They have been there both in the good times and when I needed them the most.

And last but not least, thanks to my friends that have been with me during all this years. Even though some of them refused to come for a visit in the winter because “it is too damn cold”, I cannot wait until the next time we properly meet and have a great time together.

Contents

| | |
|--|-------------|
| Abstract | i |
| Acknowledgments | iv |
| Contents | v |
| List of Figures | viii |
| List of Tables | x |
| Symbols | xi |
| Suffixes List | xii |
| Acronyms | xiii |
| Special Terms | xiv |
| 1 Introduction and Literature Review | 1 |
| 1.1 Introduction | 2 |
| 1.2 Thermodynamics of Gas Turbines | 3 |
| 1.3 Cooling Methods | 4 |
| 1.4 State of the Art | 8 |
| 1.4.1 Cooling in Gas Turbines | 8 |
| 1.4.2 Infrared Thermography for Flow Visualization | 10 |
| 1.5 Objective | 11 |
| 1.6 Thesis Outline | 11 |
| 2 Technique Selection | 12 |
| 2.1 Considered Visualization Methods | 13 |
| 2.1.1 Background Oriented Schlieren | 13 |
| 2.1.2 Planar laser imaging | 14 |
| 2.1.3 Neutrally buoyant helium bubbles | 15 |
| 2.1.4 Infrared Flow Visualization | 15 |
| 2.2 Method Selection | 17 |
| 3 Methodology | 18 |

| | | |
|----------|--|-----------|
| 3.1 | Dimensional Analysis | 19 |
| 3.2 | Heat transfer coefficient measurement using TLCs | 20 |
| 3.2.1 | Thermochromic Liquid Crystals (TLCs) | 20 |
| 3.2.2 | Heat transfer coefficient measurement | 21 |
| 3.3 | Infrared Flow Visualization | 23 |
| 3.3.1 | Infrared Spectra of Molecular Gases | 23 |
| 3.3.2 | Tracer Selection | 24 |
| 3.3.3 | Gas Detection | 25 |
| 4 | Experiment | 27 |
| 4.1 | Set-up | 28 |
| 4.1.1 | Test Rig | 28 |
| 4.1.2 | Test Samples | 31 |
| 4.1.3 | Instruments and data collection | 31 |
| 4.2 | Procedure | 34 |
| 4.2.1 | Main Flow Injection | 34 |
| 4.2.2 | Coolant Flow Injection | 35 |
| 4.3 | Post-Processing | 35 |
| 5 | Results and Discussion | 38 |
| 5.1 | Main Flow Injection | 39 |
| 5.2 | Coolant Flow Injection | 41 |
| 5.2.1 | Heated Flow, Cold CO_2 | 41 |
| 5.2.2 | Heated Flow, Hot CO_2 | 43 |
| 5.2.3 | Heated Background | 46 |
| 5.3 | Sample Comparison | 49 |
| 6 | Conclusions | 60 |
| | Bibliography | 61 |
| | Appendix | 65 |
| A | Cost | 65 |
| A.1 | Partial Costs | 65 |
| A.2 | General Cost and Taxes | 66 |
| B | Specifications | 67 |

CONTENTS

| | | |
|-----|--|----|
| B.1 | Measurement Equipment | 67 |
| B.2 | Materials | 69 |
| B.3 | Hardware and Software | 69 |
| C | Additional Information Test Objects | 70 |
| C.1 | Chemical Composition Test Objects | 70 |
| C.2 | Technical Drawing Test Object | 70 |
| D | Additional Mathematical Derivations | 72 |
| D.1 | CO_2 concentration and radiance absorption | 72 |

List of Figures

| | | |
|-----|---|----|
| 1.1 | Electricity Production by Source [1] | 2 |
| 1.2 | Schematic of a Gas Turbine [2] | 3 |
| 1.3 | Ideal Brayton Cycle [3] | 3 |
| 1.4 | Turbine Cooling Methods and Materials Evolution [4] | 4 |
| 1.5 | Internal Cooling Methods [5] | 4 |
| 1.6 | External Cooling Methods [5] | 5 |
| 1.7 | Pin Fin Cooling [6] | 5 |
| 1.8 | Turbine Vane Example [7] | 6 |
| 1.9 | Different 3D printed film-cooling geometries [8, 9] | 7 |
| | | |
| 2.1 | BOS imaging configuration [10] | 13 |
| 2.2 | Background pattern before and after a density variation [10] | 14 |
| 2.3 | Flow visualization images of a row of five round jets impinging a row of five side-by-side circular cylinders [11] | 14 |
| 2.4 | Wingtip vortex from a NACA0012 airfoil at 10 m/s [11] | 15 |
| 2.5 | Examples of Infrared Flow Visualization | 16 |
| | | |
| 3.1 | Measurement of the film cooling effectiveness (3-temperature prob- lem) in the hot gas channel using TLCs [12] | 20 |
| 3.2 | Color spaces from calibration outputs | 20 |
| 3.3 | Three-temperature problem diagram [13] | 21 |
| 3.4 | Vibrational and rotational excitation modes of carbon dioxide | 23 |
| 3.5 | Transmittance of carbon dioxide and water vapor obtained from HI- TRAN | 24 |
| 3.6 | SF_6 at different temperatures in front of a wall [14] | 25 |
| 3.7 | Difference in measured signal when using a narrow band filter [14] | 26 |
| | | |
| 4.1 | Thermochromic Liquid Crystals (TLCs) Rig | 28 |
| 4.2 | Test Set-up | 29 |
| 4.3 | Section view of test rig with film-cooling test objects attached | 30 |
| 4.4 | Images of the Test Objects and Detailed View of the Surface | 31 |
| 4.6 | Datascan 7220 16 channel measurement processor | 32 |
| 4.7 | SITRANS FC MASS 2100 | 33 |
| 4.8 | Titanium 560M | 33 |
| 4.9 | Post-processing flow diagram | 36 |

LIST OF FIGURES

| | | |
|------|---|----|
| 5.1 | Main Flow Injection at different heights, B19-P1-1.0mm BR = 1.0 . | 39 |
| 5.2 | B20-P1-1.0mm M=1.0 cold CO_2 | 41 |
| 5.3 | B20-P1-1.0mm M=1.0 hot CO_2 | 43 |
| 5.4 | B19-P1-0.5mm M=1.0 heated background | 46 |
| 5.5 | AVG, Blowing ratio = 0.5 | 49 |
| 5.6 | RMS, Blowing ratio = 0.5 | 50 |
| 5.7 | AVG, Blowing ratio = 1.0 | 52 |
| 5.8 | RMS, Blowing ratio = 1.0 | 53 |
| 5.9 | AVG, Blowing ratio = 2.0 | 55 |
| 5.10 | RMS, Blowing ratio = 2.0 | 56 |
| 5.11 | Mixing Layer Height | 57 |
| 5.12 | Lateral averaged heat transfer coefficient [13] | 58 |
| 5.13 | Laterally averaged blowing ratio [13] | 59 |
| 6.1 | Transmittance IR Window Sapphire [15] | 69 |

List of Tables

| | | |
|------|---|----|
| 6.1 | Labour Costs | 65 |
| 6.2 | Equipment Cost | 66 |
| 6.3 | Software Cost | 66 |
| 6.4 | Total Cost | 66 |
| 6.5 | NetScanner Model 9116 Specifications [16] | 67 |
| 6.6 | Datascan 7220 Specifications [17] | 67 |
| 6.7 | Rosemount 2088 Specifications [18] | 68 |
| 6.8 | SITRANS FC MASS 2100 Specifications [19] | 68 |
| 6.9 | CEDIP Titanium 560M Specifications [20] | 68 |
| 6.10 | Chemical composition of Hastelloy-X and Inconel 625 | 70 |

Symbols

| Symbol | Description | Unit |
|---------------|-------------------------------|-----------|
| S | Area | m^2 |
| A | Attenuation Coefficient | – |
| η_{th} | Thermal Efficiency | – |
| ε | Molar Attenuation Coefficient | m^2/mol |
| c | Molar Concentration | mol/m^3 |
| T | Temperature | K |
| ρ | Density | kg/m^3 |
| μ | Dynamic Viscosity | kg/ms |
| c_p | Heat Capacity | J/K |
| k | Heat conductivity | W/mK |
| \dot{Q} | Heat transfer | W |
| u | Velocity | m/s |
| L | Characterstitic Length | m |
| ξ | Adimensional Length | – |

Suffixes List

| Name | Description |
|-------------|--------------------|
| <i>w</i> | Wall surface |
| <i>m</i> | Main flow |
| <i>c</i> | Coolant flow |
| <i>f</i> | Fluid |
| <i>i</i> | Initial value |

Acronyms

| | |
|------|--------------------------------|
| AM | Additive Manufacturing. |
| EDM | Electro Discharge Machining. |
| IR | Infrared. |
| IRIV | Infrared Image Velocimetry. |
| LCs | Liquid Crystals. |
| LDA | Laser Doppler Anemometry. |
| LPBF | Laser Powdered Bed Fusion. |
| PIV | Particle Image Velocimetry. |
| SLS | Selective Laser Sintering. |
| TLCs | Thermochromic Liquid Crystals. |

Special Terms

| Name | Description |
|----------------------------------|--|
| Blowing Ratio | Ratio between the momentum of the coolant flow and the main flow. $BR = \frac{\rho_c u_c}{\rho_m u_m}$ |
| Heat Transfer Coefficient | Quantitative characteristic of convective heat transfer between a fluid medium and the surface flowed over by the fluid. $h = \frac{\dot{Q}}{S(T_w - T_f)}$ [21] |
| Reynolds Number | Ratio of inertial forces to viscous forces within a fluid. $Re = \frac{\rho u L}{\mu}$ |
| Cooling Effectiveness | Adimensional temperature of the mixed flow. $\eta = \frac{T_m - T_f}{T_m - T_c}$ |

Chapter 1

Introduction and Literature Review

1.1 Introduction

Gas turbines are used around the world to generate mechanical and electrical power because of their high power to size / weight ratio, large power range¹ and low cost of deployment². Although the presence of renewable energy sources is getting substantially bigger in the last years (Figure 1.1), the use of peak plants is currently necessary because of the high cost of large scale energy storage.

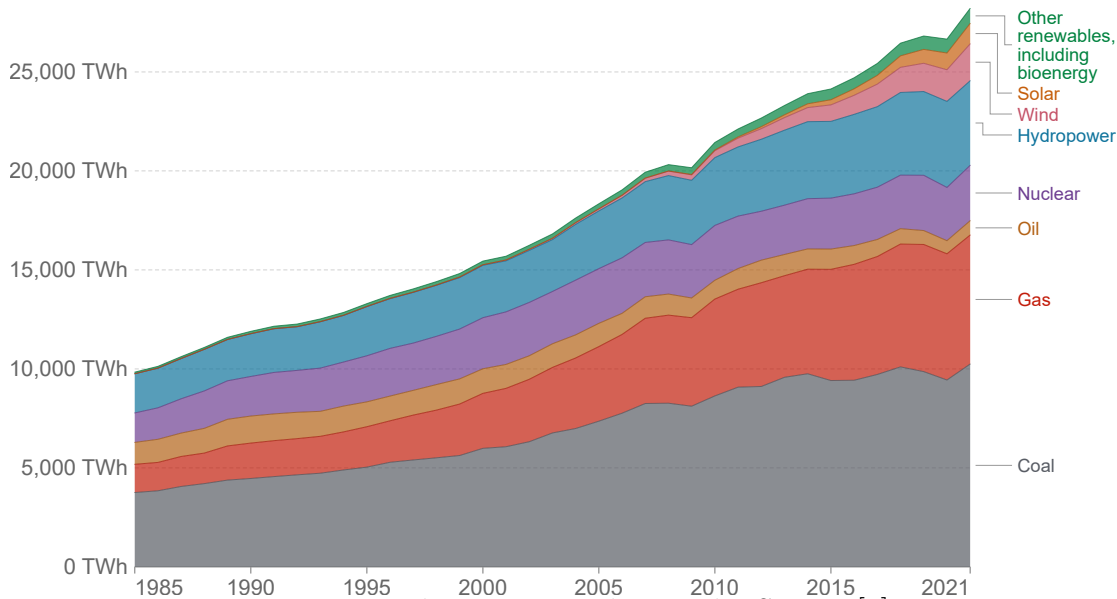


Figure 1.1: Electricity Production by Source [1]

Due to this large dependence on gas turbines, there has been extensive research on how to increase the efficiency [24]. This improvement in efficiency has led to a reduction in their operating cost and environmental impact.

This increase in efficiency has been achieved by increasing turbine inlet temperatures and pressure ratios, as well as improvements in blade aerodynamics.

These improvements have led to the development of high temperature alloys, as well as better cooling methods and thermal barrier coatings, as the working temperatures exceeded the maximum operating temperature of the vanes and blades.

¹In the energy market, gas turbines that range from 1 to 500 MW are present [22], but there are micro-turbines with power as low as 25 kW[23]

²Compared to other power generation systems such as nuclear or coal plants

1.2 Thermodynamics of Gas Turbines

Gas turbines are composed of three main elements: compressor, combustion chamber and turbine. The first section of the gas turbine, composed of the intake and compressor, is the so called cold section. Its main purpose is to compress the flow before the combustion. The second section, composed of the combustion chamber, turbine and exhaust is the so called hot section. Its purpose is to extract the chemical energy stored in the fuel and transform it into mechanical energy with the use of the turbine. (Figure 1.2)

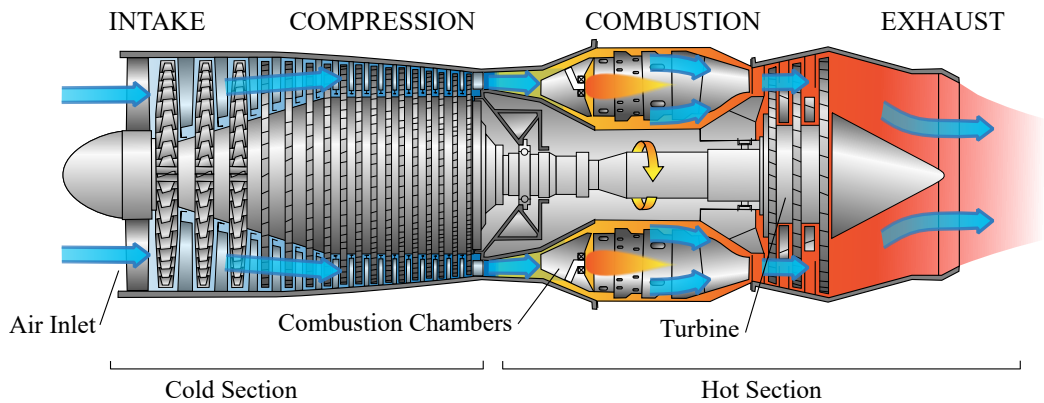


Figure 1.2: Schematic of a Gas Turbine [2]

The operation of the gas turbine can be idealized by the brayton cycle, which is composed of an isentropic compression, isobaric heat addition, isentropic expansion and an isobaric heat rejection (Figure 1.3).

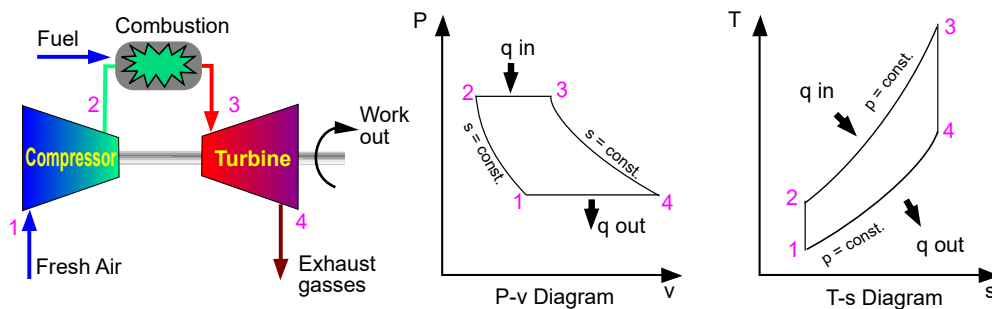


Figure 1.3: Ideal Brayton Cycle [3]

Following the appropriate thermodynamic steps, the efficiency of the cycle is given by Equation 1.1:

$$\eta_{th} = 1 - \frac{T_4}{T_3} \quad (1.1)$$

As seen in Equation 1.1, the higher the turbine's inlet temperature, the higher the efficiency of the gas turbine. However, the turbine inlet temperature can not be arbitrarily high as it has to be withstood by the turbine. As so, there is a high interest in developing methods that allow for a higher turbine inlet operating temperature (Figure 1.4).

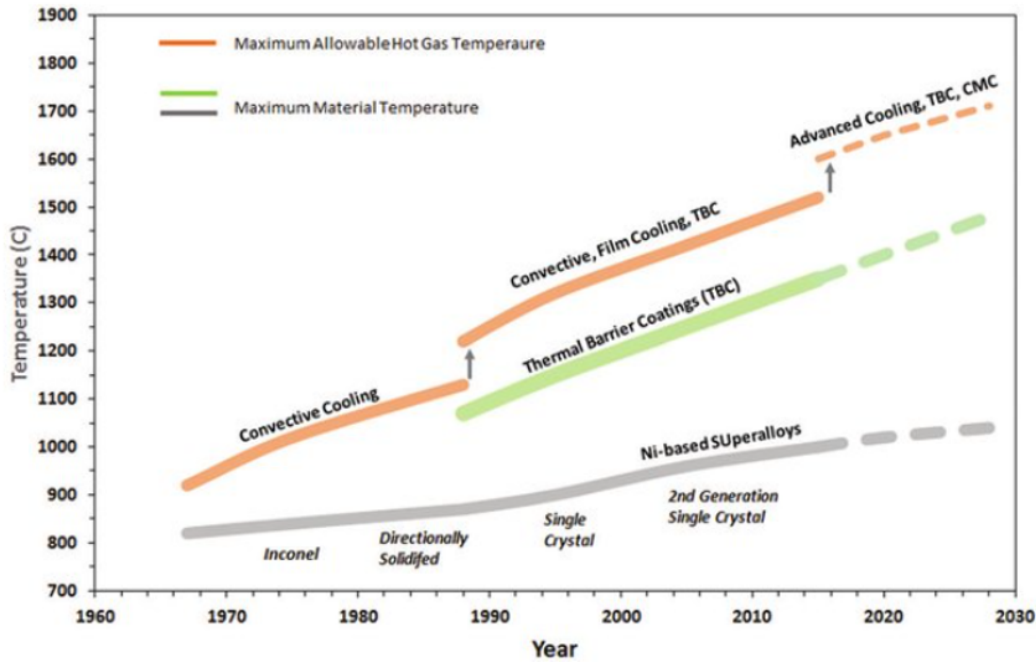
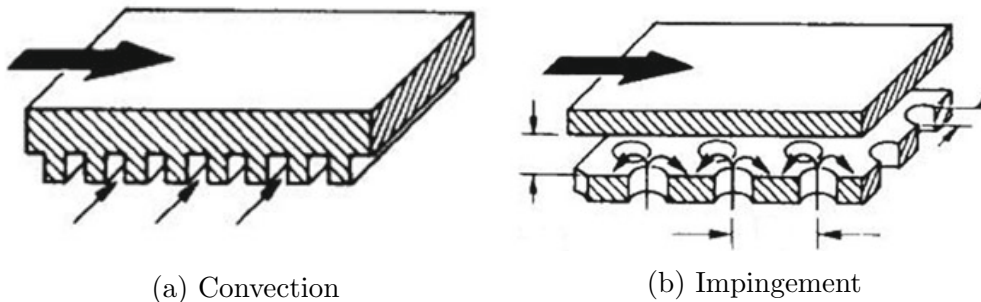


Figure 1.4: Turbine Cooling Methods and Materials Evolution [4]

1.3 Cooling Methods

Turbine blade cooling is divided into two main categories: internal and external methods. Internal methods are based on transferring the heat to the coolant flow that circulates inside the vane (1.5). External methods are based on generating a protective layer around the blade to shield it against the hot main-flow (1.6). [5]



(a) Convection

(b) Impingement

Figure 1.5: Internal Cooling Methods [5]

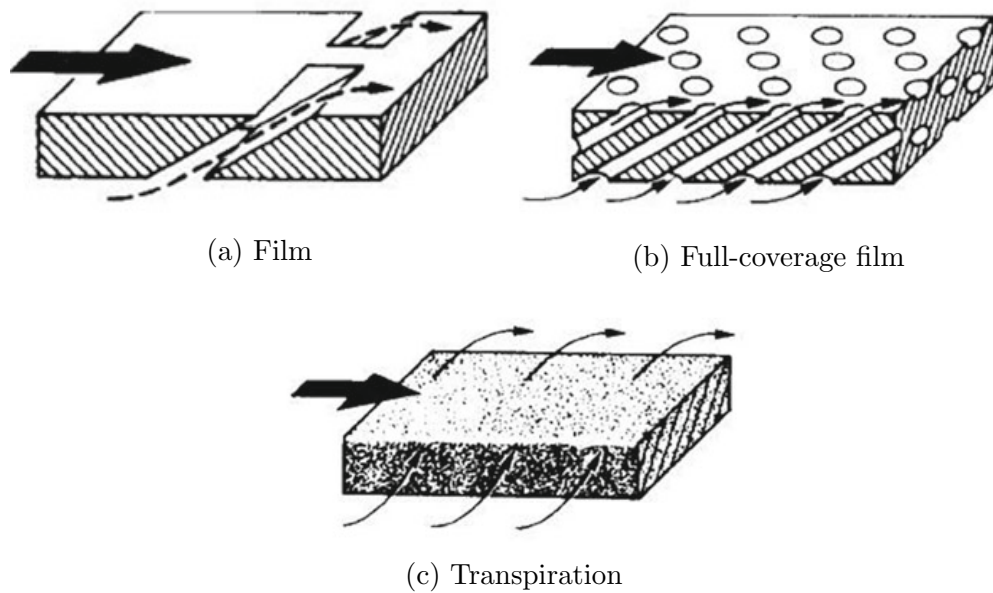


Figure 1.6: External Cooling Methods [5]

Convection Cooling

Cooling air channels are designed inside the vane or blade, removing heat through the walls. Usually, the internal passages go from the hub to the blade tip.

Impingement Cooling

It is an advanced form of convection cooling. In this method, small holes are used to blast the air into the inner surface of the airfoil. This technique is reserved to selected regions, such as the leading edge, that require higher cooling.

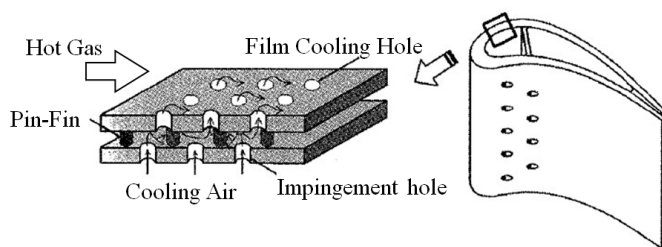


Figure 1.7: Pin Fin Cooling [6]

Other advanced forms of convection cooling such as pin-film cooling also exist. They can be used in conjunction with other techniques such as impingement and film cooling (Figure 1.7).

Film Cooling

Film cooling is based on using cooling air as an insulating medium. The coolant air is injected to the main flow in a way that it creates an insulating layer. It can be used in a localized or full-coverage configuration.

Transpiration Cooling

Transpiration cooling is an advanced form of film cooling, where cooling holes are substituted by a porous wall. The advantages of this method is that it generates a more consistent insulating layer and, as the coolant has to be forced through the wall, the heat transfer coefficient is quite high.

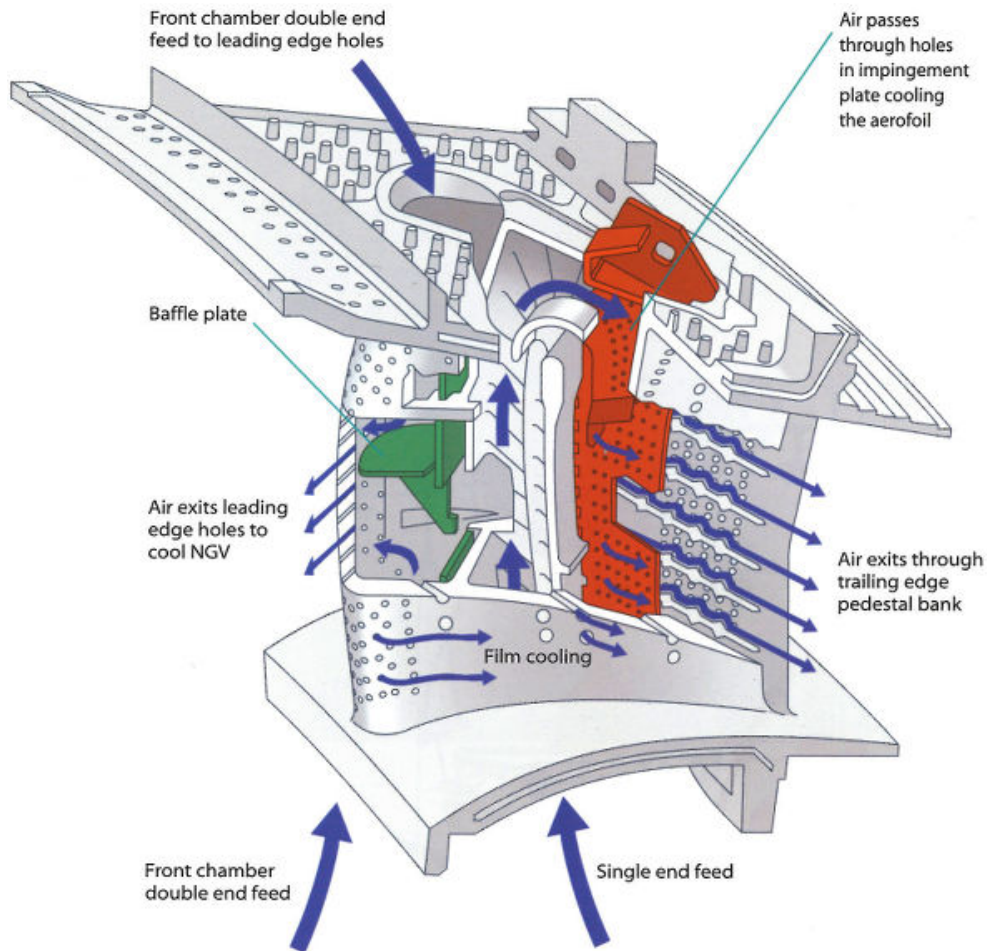


Figure 1.8: Turbine Vane Example [7]

As the turbine inlet temperature has been increasing in a yearly basis, cooling methods are continuously evolving. In the current time period, multiple cooling methods are used simultaneously in order to keep up with the increasing operating demands.

As can be seen in Figure 1.8, this generates quite complex geometries that are manufactured in hard to machine materials. This makes the process of manufacturing this components quite expensive. Recent advancements in Additive Manufacturing (AM) have made possible to 3D print this geometries using super-alloys on commercially available machines (Figure 1.9).

Moreover, is it possible to directly generate porous materials when printing if the specific printing parameters are selected. One of this methods consist on

increasing the hatch distance so that defects in the matrix are generated.

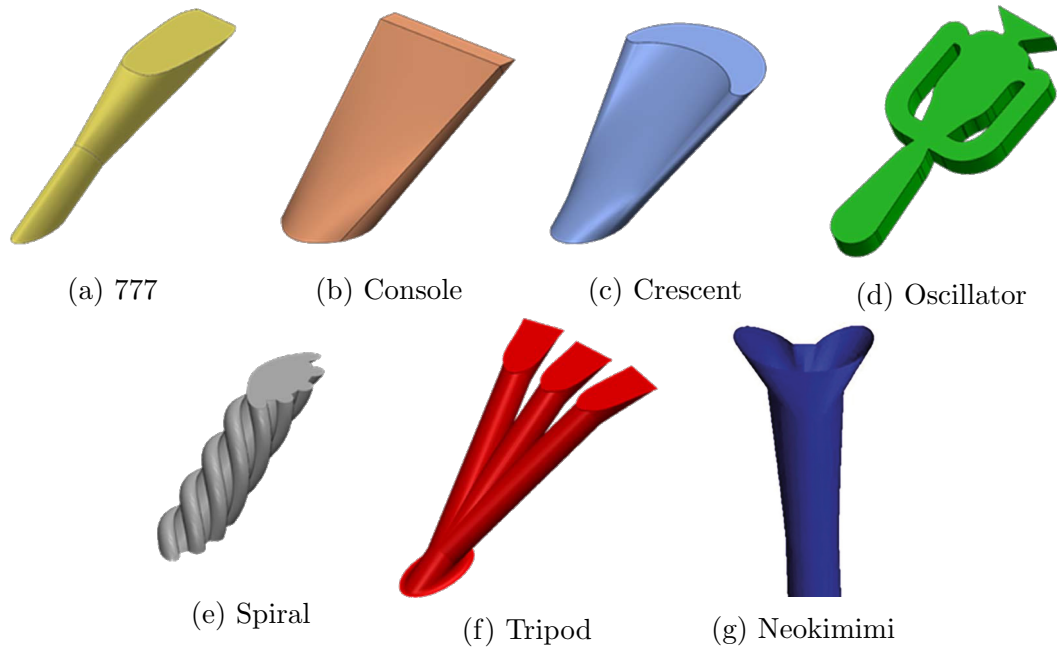


Figure 1.9: Different 3D printed film-cooling geometries [8, 9]

Although the structural strength of the part is lower compared to single crystal super-alloys, as greater cooling can be achieved, it is a viable manufacturing method³. Additionally, as there is no need for complex manufacturing process that involve a high initial cost, the testing can start early on in the development phase.

³As of today, structural integrity in 3D printed parts is not sufficient for the blades due to the high centrifugal forces

1.4 State of the Art

1.4.1 Cooling in Gas Turbines

Research on film-cooling and transpiration-cooling in gas turbines started in the early 1950's. At the time, the conventional method for turbine blade cooling was internal convection cooling. This presented the disadvantage that, if the gas-to-blade and blade-to-coolant heat transfer coefficient are the same⁴, the wall temperature lies between the gas and coolant temperature. [25]

The use of ceramic coatings with sufficient thickness as thermally insulating materials was not possible as they did not provide enough structural strength. Therefore, the use of air to generate an insulating layer was suggested as is low thermal conductivity would lead to a reduced heat transfer.

Eckert and Esgar studied the effect of forming an insulation layer in between the blade surface and the hot main flow. Film and transpiration cooling were studied. Transpiration-cooling generated more effective and uniform cooling with respect to film-cooling. However, fabrication techniques had to be developed to manufacture high-strength porous structures, with controlled permeability.

Film-cooling

The main parameters that govern the performance of this cooling methods are: hole diameter, hole shape, hole spacing, number of holes, injection angle and blowing ratio.

Different studies have been conducted on this parameters to improve the efficiency and coverage of film-cooling. The use of shaped holes have been studied by Bell et al. and Bunker, showing that altering the outlet shape of the hole can lead to a cooling enhancement.

The use of fan shape holes has been extensively studied, as they offer better lateral-coverage and less penetration because of its diffused geometry (Gritsch et al.). Evolutions of the fan shaped and double-jet concepts have been studied. 10. showed that NEOKIMIMI-type holes is more advantageous for the formation of anti-vortex structures (Figure 1.9g).

Given that most of the advanced film-cooling designs are expensive and difficult to manufacture using conventional manufacturing techniques such as milling or Electro Discharge Machining (EDM), some researchers focused on more easily to manufacture geometries such as cratered holes. Kalghatgi and Acharya showed that the use of a contoured crater weakens the kidney-pair vortex by generating a pair of counter rotating vortexes, leading to the coolant jet being closer to the wall and reduced mixing.

However, with the advance in AM, more complex geometries can be manufac-

⁴It is difficult to have higher blade-to-coolant heat transfer coefficient because of the high velocities of the main flow

tured using super alloys. As AM allows the creation of more intricated internal geometries that were prohibitively expensive or not possible to manufacture with conventional manufacturing (Figure 1.9).

Snyder and Thole showed that Additive Manufacturing can produce this complex cooling designs using the laser powder bed fusion method. Moreover, some geometry considerations for printing were stated.

Transpiration-cooling

The biggest drawback of film-cooling is the non-uniformity that is created in the cooling due to the presence of discrete holes. Transpiration-cooling removes this problem by using a porous structure to generate a more uniform protective layer.

There have been studies on transpiration-cooling dating from the 1950's. Eckert and Esgar state the benefits of this form of cooling, but remark that it was not viable to make this structures. Metallic foam was used to generate the porous test objects. Although it achieves very high porosity, it has poor mechanical properties and is a slow manufacturing process.

Huang et al., in a study focused in sintered porous plates, found that increasing the thermal conductivity reduced the temperatures and non-uniformities of the protected surfaces. It also was found that surface temperatures decreased significantly for even a small blowing ratio.

Other manufacturing method that can be used to generate a porous material is lamination (Nealy and Reider). With this process, thin layers are manufactured with micro-channels and welded. Although this method has advantages such as being able to control the local porosity and presents higher strength, it needs an assembly process which adds complexity to the manufacturing and is time consuming.

Huang et al. showed that, having alternated regions made porous (perforated) and solid increased the ultimate tensile strength by as much as 440% with respect to a sintered plate. While this test objects had similar performance at $BR = 0.02$, the sintered porous plate had better cooling effectiveness at $BR = 0.03$.

During the work of previous students working at Siemens Energy, the downstream cooling effectiveness and heat transfer coefficient are measured by using TLCs. The test objects studied were manufactured by Laser Powdered Bed Fusion. In order to have a better understanding on the flow behaviour of the porous test objects and its relation to the heat transfer coefficient and blowing ratio, the project continued by performing flow visualization using infrared thermography.

1.4.2 Infrared Thermography for Flow Visualization

The qualitative detection of gases themselves by thermal imaging is a rather new application. One of the first reported cases of use of this technique is Vollmer and Klaus-Peter. In this study, the vortical flow at the wingtip of an airplane was seeded with sulfur hexafluoride and recorded with an IR camera. Best results were achieved with a clear sky background. This technique is later used by Tiddens et al. to visualize the flow of an open volumetric receiver of a solar tower. Infrared Image Velocimetry (IRIV) is used to get qualitative vector fields of the flow.

Sandsten et al. studied N_2O plumes. By receiving the incoming light through a cell containing the studied gas at high concentration so that almost no light can pass through and then through a variable neutral-density filter. The imbalance introduced between both measures gives the concentration of the gas of interest in the plume. This method removes the measured effect from other gases that might be present.

Narayanan et al. used infrared thermography to visualize the flow generated by axi-symmetric jets impinging on plates. The visualization technique involves the use of a heated background at a different temperature than the flow. An initial image is taken without a seeder gas to perform image subtraction and highlight the region of interest. Variants of this technique have been used to study the behavioral analysis of turbulent exhale flows (Transue et al.) and study the release of gaseous CO_2 during champagne serving (Bourget et al.).

Heated seeders can also be used for flow visualization, removing the need of a heated background. Yoon et al. analyze the flow generated by nozzles of the air-jets used for explosive detection.

In the present study, infrared thermography is used to visualize the cross-flow interaction in transpiration-cooling. Because of the small nature of the pores in transpiration-cooling, other visualization techniques such as Particle Image Velocimetry (PIV) that rely on the use of particles as a seeder can not be used. Other techniques such as Laser Doppler Anemometry (LDA) present also difficulties as the seeder build-up when flowing through the sample will change its characteristics and cause irreparable damage to it.

1.5 Objective

The main objective of this work is to evaluate an appropriate flow visualization method to visualize the downstream flow behaviour on additively manufactured porous structures.

As the porous diameter is in the order of $100 \mu m$, additional care must be taken to select the appropriate method to not interfere significantly with the results or damage the test samples.

Once a specific methodology has been selected, it will be used to compare the differences between the test samples available and correlate the flow behaviour with the performance of the samples obtained in previous studies

1.6 Thesis Outline

The thesis is structured as follows. In Chapter 2, different visualization techniques will be proposed. In Chapter 3, the theory regarding TLCs and Infrared Flow Visualization will be explained. Chapter 4 focuses on the set-up, procedure and post-processing of the results. Chapter 5 presents the results from the different forms of flow visualization tested and shows a comparison between the different samples that were tested. Conclusions based on the obtained results are stated in Chapter 6.

Chapter 2

Technique Selection

In this chapter, different visualization methods will be discussed. The advantages and drawbacks of those will be discussed in detail. A final note will be added on why active IR gas tracer was selected among those techniques.

As methods that rely on point measurements for the visualization involve a long time of working to get map results, they are not considered for the visualization.

2.1 Considered Visualization Methods

2.1.1 Background Oriented Schlieren

Background Oriented Schlieren (BOS) belongs to the family of refractive index measurement techniques. BOS uses a dotted background to detect the differences in the refractive index due to pressure and temperature changes.

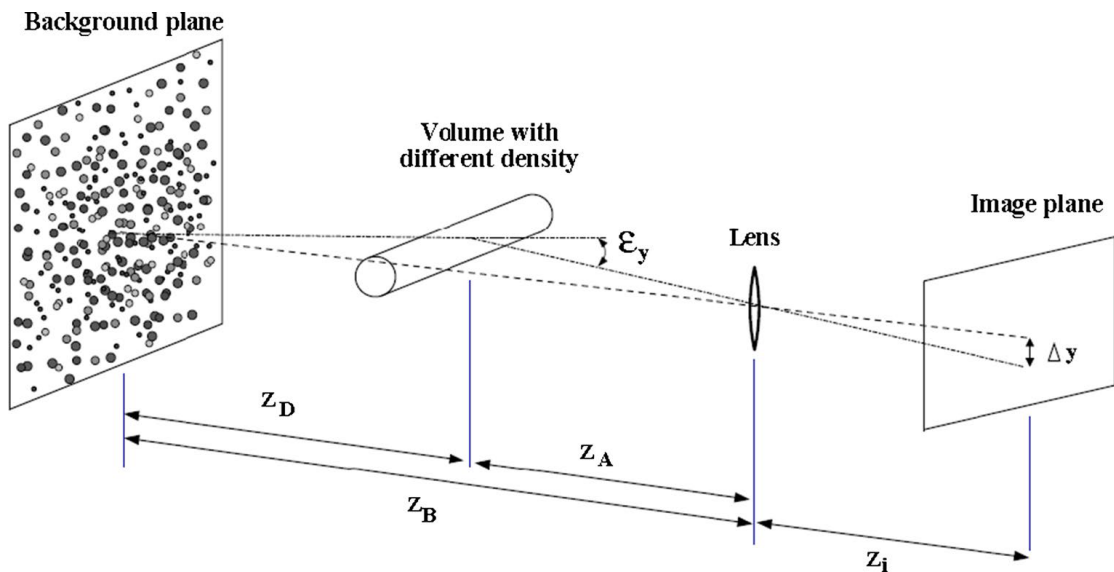


Figure 2.1: BOS imaging configuration [10]

Compared to the older Schlieren photography, shadowgraphy and interferometry, the use of the dotted pattern eliminates the need of expensive mirrors and complicated configurations [10].

As can be seen in Figure 2.2, the positions of the background dots is modified by the change of density in the fluid. Obtaining the displacement correlation between both images, it is possible to highlight the flow patterns.

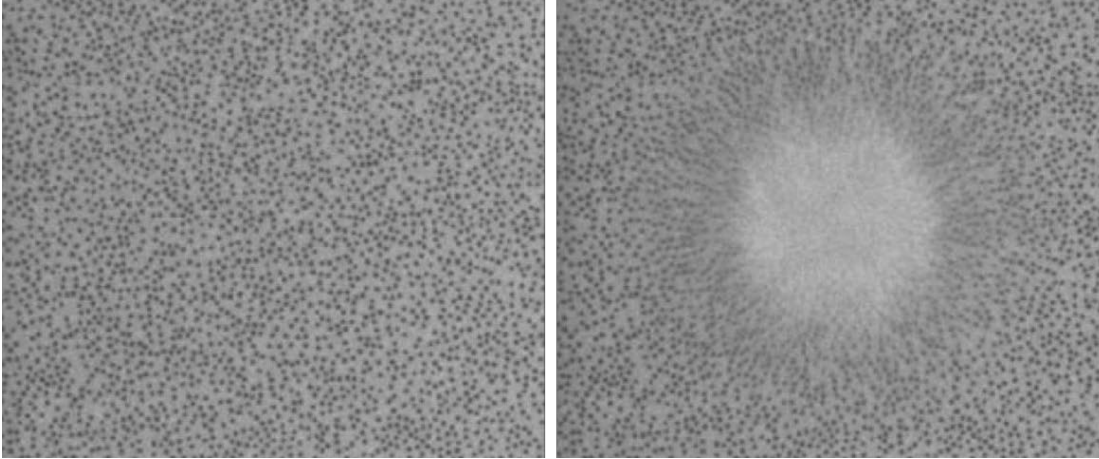
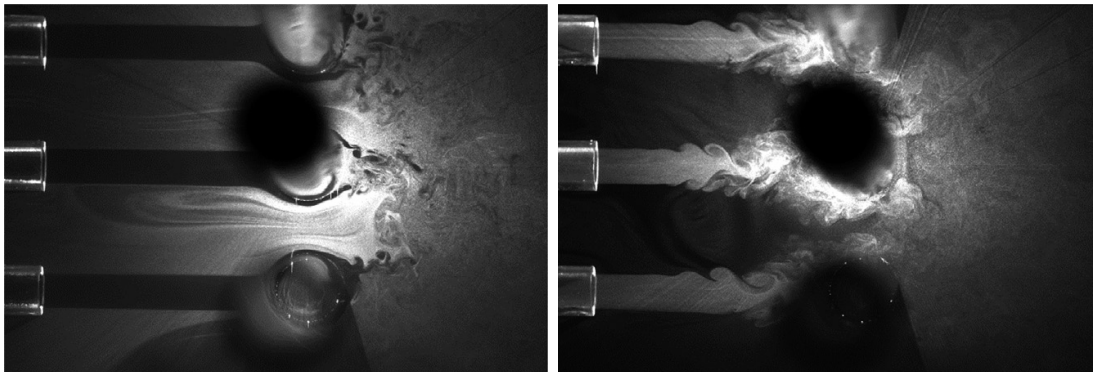


Figure 2.2: Background pattern before and after a density variation [10]

2.1.2 Planar laser imaging

This method is based on illuminating a thin part of the flow by means of a planar laser sheet. Seeding the flow with solid particles or smoke, the flow details are revealed in the illuminated slice of the flow.



(a) Fully laminar jet, $Re_{Dj} = 730$, using the external seeding circuit (b) Semiturbulent jet, $Re_{Dj} = 2780$, employing the internal seeding circuit

Figure 2.3: Flow visualization images of a row of five round jets impinging a row of five side-by-side circular cylinders [11]

As this methods allow the experiment operator to just focus on a certain slice of the flow, it allows a fine control of the region of interest for the experiment. Additionally, the flow behaviour and transition from laminar to turbulent is easily recognizable from the results obtained.

Moreover, it is possible to obtain accurate flow velocity fields using Particle Image Velocimetry (PIV). Taking pictures of the flow at different times, the velocity distribution can be obtained from the relative movement of the particles.

The main drawback of this method is that the seed material may coat the porous structure (if it is injected in the coolant) and, many of the seedants used in flow visualization and velocimetry can pose safety concerns [40].

2.1.3 Neutrally buoyant helium bubbles

Bubbles made of helium enclosed in a liquid film are used as a tracer to follow the flow. The main benefit of this bubbles is that they have low inertia and also are approximately buoyant. This directly allows them to follow the flow in a more accurate way. An additional benefit is that they generate better streamlines than solids particulates or smoke, as they present a higher contrast.



(a) Correct exposure of bubbles (b) Manipulated image to highlight vortex
Figure 2.4: Wingtip vortex from a NACA0012 airfoil at 10 m/s [11]

The main problem of this method for our application is that they have to be injected upstream of the main flow (as they cannot pass through the porous sample). This limits the visualization as, in order to get a clear boundary between the coolant and the main flow, they should be close to the ground just before the coolant injection in order to follow the streamline of the boundary.

This technique is more effective when the test objects that are placed in the middle of the test section.

2.1.4 Infrared Flow Visualization

Off-surface flow phenomena can be visualized using an infrared imaging system and a IR active tracer gas. This method is almost equivalent to using smoke for flow visualization, with the difference that rather than using a conventional camera, an IR camera must be used.

The method consists on injecting a gas that has strong absorbing and emitting characteristics in the infrared spectrum, such that its presence will be revealed in the recordings.

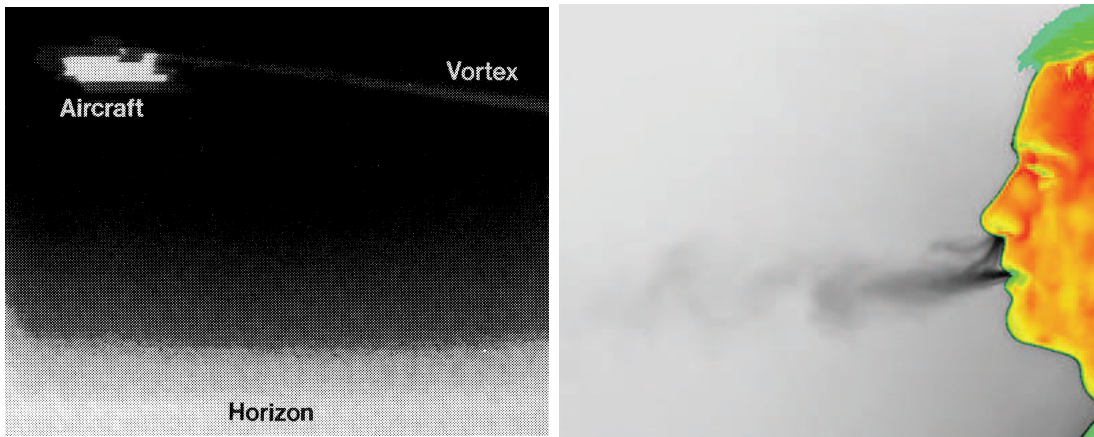
(a) Wing tip vortex seeded with SF_6 [41](b) Exhaled CO_2 [37]

Figure 2.5: Examples of Infrared Flow Visualization

As stated in [34], the basic requisites to select the seeding gas are the following:

- Good absorbing / emitting characteristics in a particular wavelength that can be detected by an IR camera
- Distinguishable from other present gases at that wavelength
- Non toxic or harmful to the environment
- Low concentration in the atmosphere

This technique allows the tracer to be injected in the coolant flow but, as the signals produced by it are generally faint, additional care must be taken in order to obtain acceptable results. Moreover, as the pattern visualized is the projection of the tracer, flow details that are not found on the border between the tracer and the air are obscured.

2.2 Method Selection

Among the presented methods, the selected methods for the visualization were “Planar Laser Imaging” and “Infrared Flow Visualization”, where the most promising method was the later because of the possibility of injecting the tracer as coolant without damaging the porous structure.

Both methods were considered relevant as, while the first one allowed to have a detailed flow visualization of the main flow on a thin slice of the flow (including the boundary between coolant and main flow), the second allowed to directly measure the quality of the coverage of the coolant.

With regards to neutrally buoyant helium bubbles, the method was not considered because of the inherent difficulty of visualizing the boundary between the main and coolant flow. Planar laser imaging was thought to be a better method because the tracer can have a bigger coverage on the flow and the required systems / instrumentation were already present in the laboratory.

Regarding Background Oriented Schlieren, the method should obtain similar results compared to Infrared Flow Visualization. As the later one allowed to have greater measurement resolution¹, it was considered better.

As can be seen in Figure 2.3, using small droplets as a tracer and selecting an appropriate exposure time, is possible to get a streak or stream like visualization of the flow. This facilitates the interpretation of the results, as with this type of imaging it is simple to discern the flow characteristics and turbulence, being able to closely follow the eddies in all the recorded areas (and not only in the borders). The use of PIV was not considered as the equipment needed to record the flow at a sufficiently high rate was not available.

As the wind tunnel used is an open tunnel whose exhaust is located in the laboratory, additional care must be taken in the selection of the seeded material because of safety reasons. Solid particle seeders or smoke were then discarded for this reason. The selected seeder was liquid seeding (concretely water fog), as it was easy to implement and it could be run continuously without having to clean the rig because of residue build up or arise any safety concerns in the lab environment.

Although this technique was promising, some tests were conducted and it was concluded that the technique was unreliable. It was not possible to obtain a good coverage of droplets in the measuring part of the set-up. For this reason, it was decided to not use this technique to a greater extent.

¹The recorded pixels directly contain the information about the density of coolant, rather than having to compute the displacement of dots

Chapter 3

Methodology

3.1 Dimensional Analysis

Dimensional analysis is the study of the relationships between the different physical parameters of a problem. In the case of film-cooling, the Reynolds number and blowing ratio are the ones that relate to the geometry and flow properties.

The Reynolds number is an adimensional number that is defined as the ratio of inertial and viscous forces within a fluid (Equation 3.1) and is related to the turbulence of the flow.

$$Re = \frac{\rho u L}{\mu} \quad (3.1)$$

In the studied case, the Reynolds number is set to 25000.

The blowing ratio is an adimensional number that is defined as the ratio of momentum of the coolant and main flow (Equation 3.2).

$$BR = \frac{\rho_c u_c}{\rho_m u_m} \quad (3.2)$$

In the studied case, blowing ratios 0.5, 1.0 and 2.0 will be tested to analyze the effect of this parameter on the heat transfer and flow characteristics.

Additionally, non-dimensional coordinates can be used to reference the position with respect to the test object (Equation 3.3).

$$\xi_x = \frac{x}{L} \quad (3.3)$$

Where L is the characteristic length of the channel. In the case of film-cooling, it is the diameter of the hole while in transpiration-cooling, it is the width of the porous part of the test object.

Summarizing, the cooling effectiveness and heat transfer coefficient dependency is represented by Equation 3.4

$$h, \eta = f\left(\frac{x}{L}, Re, BR\right) \quad (3.4)$$

3.2 Heat transfer coefficient measurement using TLCs

3.2.1 Thermochromic Liquid Crystals (TLCs)

Liquid Crystals (LCs) are a state of matter that has properties that are in between conventional liquids and solid crystals. They present a phase change that is dependent on different parameters such as temperature, concentration, etc. In the case of TLCs, the liquid crystal phase is dependent on the temperature [42].

They show different colors by reflecting incident white light. If applied in thin films, they reflect bright colors after a threshold temperature. After this threshold temperature, their color changes with the temperature, passing through the colors of the visible spectrum sequentially before turning colorless again.

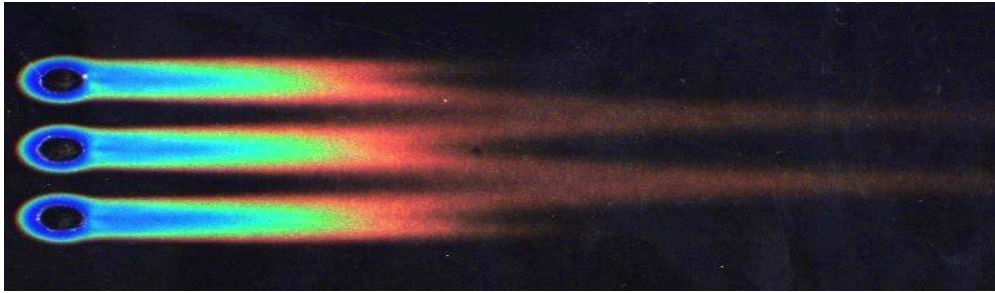
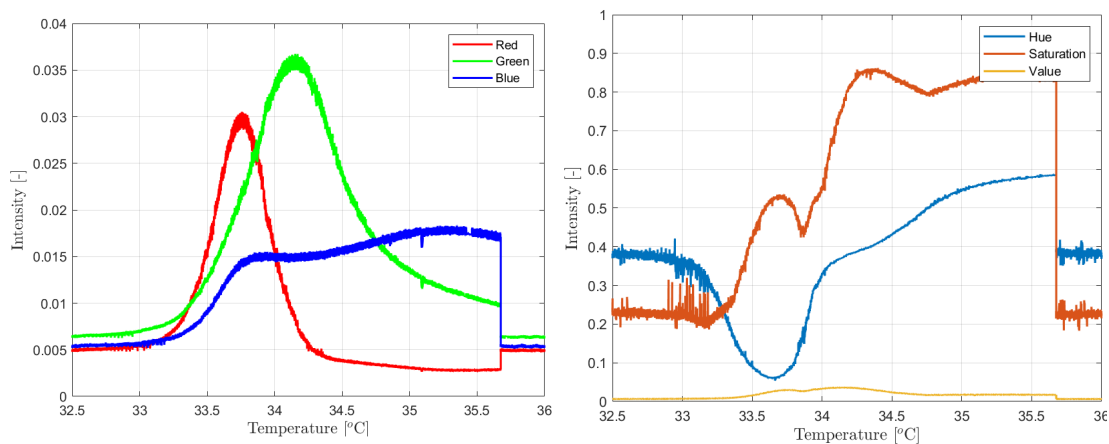


Figure 3.1: Measurement of the film cooling effectiveness (3-temperature problem) in the hot gas channel using TLCs [12]

In order to calibrate the TLCs sheet response, it is placed over a body of constant temperature and its response is recorded through the acrylic plate that was used as the top plate of the test rig.



(a) RGB values depending on temperature (b) HSV values depending on temperature

Figure 3.2: Color spaces from calibration outputs

3.2.2 Heat transfer coefficient measurement

During a forced convection process, the heat transfer is described by newton's law of cooling (Equation 3.5).

$$\frac{\dot{Q}}{S} = h \cdot (T_f - T_w) \quad (3.5)$$

For the case studied, film-cooling and transpiration-cooling, the experiment becomes a three-temperature problem (Figure 3.3).

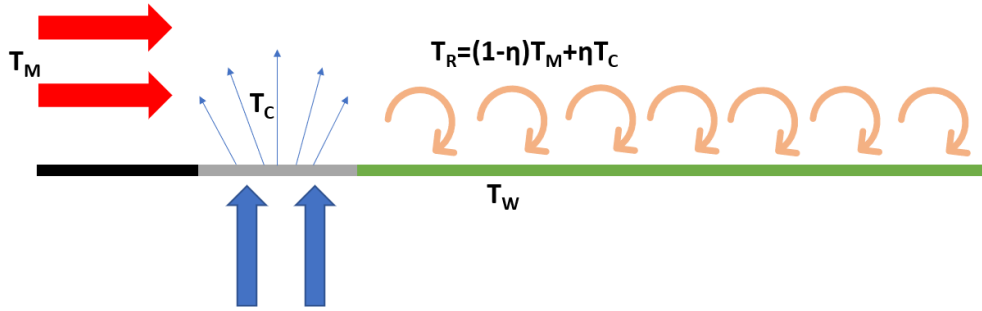


Figure 3.3: Three-temperature problem diagram [13]

By the definition of the cooling effectiveness, the fluid / reference temperature becomes (Equation 3.6):

$$T_f = (1 - \eta)T_m + \eta T_c \quad (3.6)$$

Regarding the study plate, the one-dimensional transient heat conduction equation over a semi-infinite solid (Equation 3.7) is assumed in order to obtain the heat transfer coefficient and cooling effectiveness ¹.

$$\rho c_p \frac{\partial T}{\partial t} = k \frac{\partial^2 T}{\partial z^2} \quad (3.7)$$

Using as boundary conditions:

- Uniform initial temperature

$$T(z, 0) = T_i \quad (3.8)$$

- Semi-infinite assumption ²

$$\lim_{t \rightarrow \infty} T(z, t) = T_i \quad (3.9)$$

¹ k, ρ, c_p are assumed constant

²Physically it means that the bottom of the plate never changes temperature as is located at an infinite distance. This assumption is correct if the length of the experiment is short

- Convective heat transfer at the top

$$-k \frac{\partial T(0, t)}{\partial z} = h(T_w - T_f) \quad (3.10)$$

By applying the boundary conditions to the heat transfer equation and reorganizing the terms, Equation 3.12 is obtained:

$$\beta = h \sqrt{\frac{t}{k \rho c_p}} \quad (3.11)$$

$$T_w = T_i + (1 - \exp(\beta^2) \operatorname{erf}(\beta)) \cdot (\eta T_c + (1 - \eta) T_m - T_i) \quad (3.12)$$

As we have 2 unknowns in the equations, there are three methods that can be used to solve it:

- Two-peaks method: One experiment is performed and two temperatures are obtained from the TLCs by using 2 different known points. As seen in Figure 3.2a, green and red maximum value can be used. However, this method gave problems as the uncertainty was too high due to the peaks being too close together.
- Hue Method: One experiment is performed and, using a correlation that relates hue with temperature (Figure 3.2b), curve fitting is used to get the optimal values for the coefficients. This method was tested but the results had low repeatability due to reflections.
- Two-tests method: Two experiments are performed to get 2 different known temperatures. Either the green or red peak could be used as known points (Figure 3.2a). This was the selected method as the solution was numerically more stable.

3.3 Infrared Flow Visualization

As mentioned in Section 2.1.4, infrared flow visualization is based on injecting an IR active gas to highlight a certain region or feature of the flow. In order to implement this technique, special care must be taken to ensure that the selected tracer gas is easily distinguishable from the gases already present in the atmosphere.

To achieve that, the tracer needs to have the following characteristics:

- Not be present in high quantities in the atmosphere
- Be the only IR active gas in the selected wavelength range
- Have a region of activity within the range of IR cameras

Additionally, the gas cannot be toxic or harm the environment as that will involve additional safety measures that will increase the complexity of the experiment. As a cost savings perspective, the component should be cheap.

Although it is possible to obtain quantitative measurements from the IR imaging of gases, there are some associated problems (Section 3.3.3) that may render this impossible at practical effects. In most of the cases, the flow visualization is made in a qualitative mode (Vollmer and Klaus-Peter).

3.3.1 Infrared Spectra of Molecular Gases

One of the known methods for light absorption or emission by atoms is due to electronic excitation. In this process, photons of light are absorbed by an electron when it raises to a higher energy state (or released when it returns to a lower one).

However, this phenomenon happens mostly in the visible or ultraviolet part of the spectrum, having little to no effect in the infrared. In the case of infrared spectrum, vibrational and rotational excitations of molecules leave characteristic patterns in the infrared spectrum.

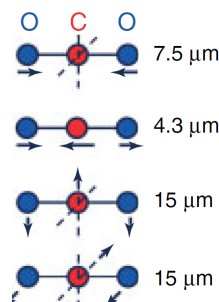


Figure 3.4: Vibrational and rotational excitation modes of carbon dioxide

Using the semiclassical description of those vibrational and rotational modes, chemical bonds are treated as springs and atoms as punctual masses. In order for these modes to absorb IR radiation, the electric dipole moment of the molecule must change.

Using CO_2 as an example, in Figure 3.4 it is possible to see how, even though there is a possible vibrational mode at $7.5 \mu m$, it does not absorb infrared radiation as the electric dipole moment of the molecule does not change due to its symmetry.

3.3.2 Tracer Selection

The main spectral absorption features present in air are caused by carbon dioxide and water vapor (Vollmer and Klaus-Peter). Even though CO_2 is already present in the atmosphere, its concentration is low enough to be considered as a possible tracer. As stated by Tiddens et al., carbon dioxide it fulfills all the requirements.

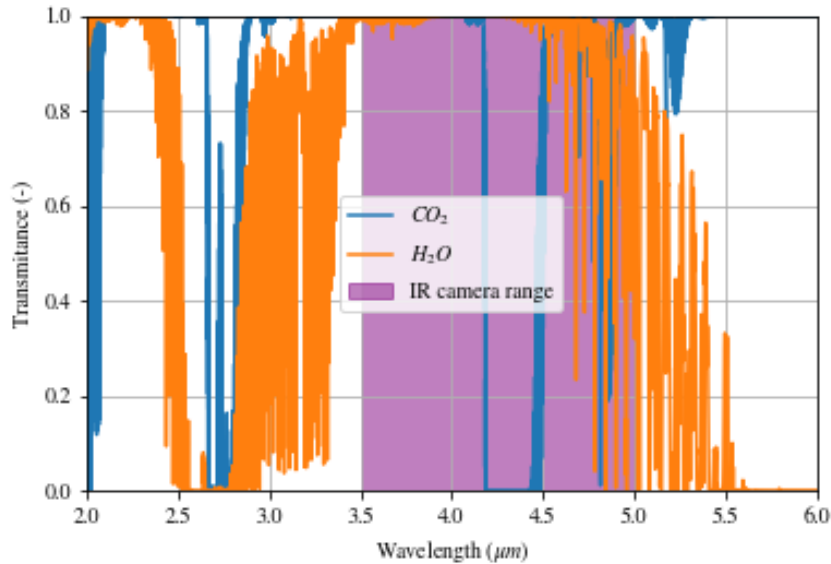


Figure 3.5: Transmittance of carbon dioxide and water vapor obtained from HITRAN

As it can be seen in Figure 3.5, carbon dioxide has a low transmittance region around $4.24 \mu m$, within the range of the infrared camera and far apart from other IR active gases present in the atmosphere.

Taking into account that CO_2 is not considered harmful to the environment³ and also has a low associated cost, it is hereby chosen as the tracer gas that will be used for the visualization.

³In the used dose

3.3.3 Gas Detection

When the gas is injected, its interaction with the IR radiation makes the flow visible in the recordings. As stated by Vollmer and Klaus-Peter, there are three main mechanisms for the gas molecules to interact with IR radiation:

- **Absorption:** The gas molecule is at a low state and absorbs the incoming radiation
- **Emission:** IR radiation is emitted as the gas molecule is at an excited state
- **Scattering:** The gas molecules absorb and re-emit suitable IR radiation. Additional IR radiation is detected compared to the case with no gas

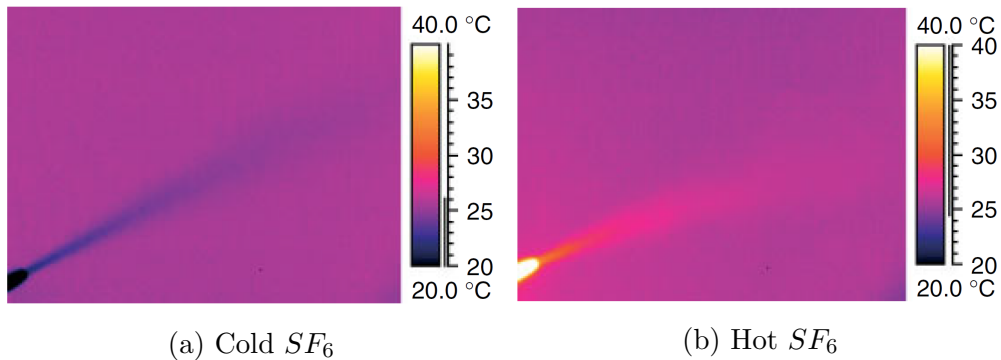


Figure 3.6: SF_6 at different temperatures in front of a wall [14]

In Figure 3.6 it is seen how injecting the tracer gas at different temperatures may change the way it interacts with the background, from absorbing the background radiation at low temperatures to emitting additional radiation when it is heated.

Scattering increases the difficulty of obtaining quantitative measurements from the IR imaging. If other hot objects are present close to the gas, the surroundings will emit IR radiation that will alter the signal strength. In a case of study with a cold gas and a hot background, it could happen that (even though the gas should absorb the background radiation) it is also absorbing the foreground one and re-emitting it, appearing as an emitter.

As the surroundings affect the results, if one wants to obtain quantitative data from an experiment with significant scattering the individual temperatures, emissivities, radiance pattern, etc, must be known. This makes obtaining quantitative results practically impossible in some cases. It is possible to reduce this effect by shielding the observed gases from hot objects, this is practically impossible in some situations in which the working region of the experiment needs to be small or the shielding may affect the flow. In Transue et al. it is possible to see a good example on how to achieve this, by using a heated background and placing any object that may contribute significantly far away from the place in which the test is conducted.

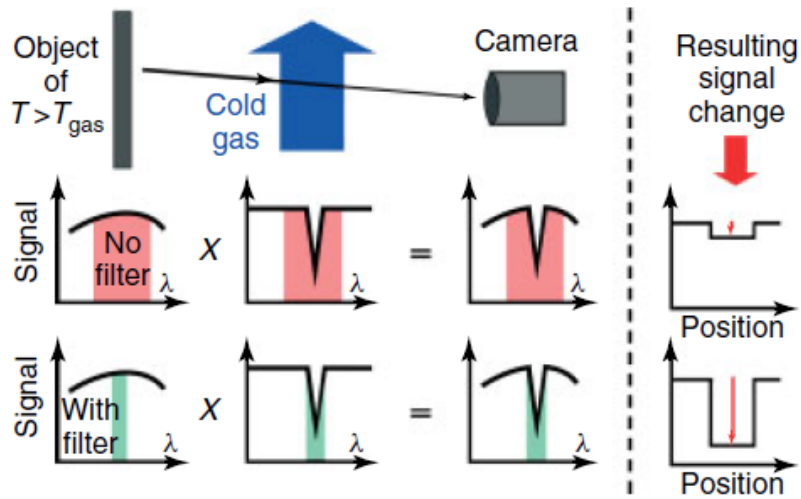


Figure 3.7: Difference in measured signal when using a narrow band filter [14]

In order to increase the sensitivity of the camera for the injected tracer, a narrow band filter could be used to increase the relative signal of the gas compared to the injection (Figure 3.7). For this experiment, a $4.26 \mu\text{m}$ narrow band filter is positioned in the filter wheel of the IR camera.

Chapter 4

Experiment

4.1 Set-up

4.1.1 Test Rig

Thermochromic Liquid Crystals (TLCs)

In order to get the measurements of the heat transfer coefficient and cooling effectiveness, a test rig with an acrylic top was used in order to get optical access to the TLCs sheet (Figure 4.1).

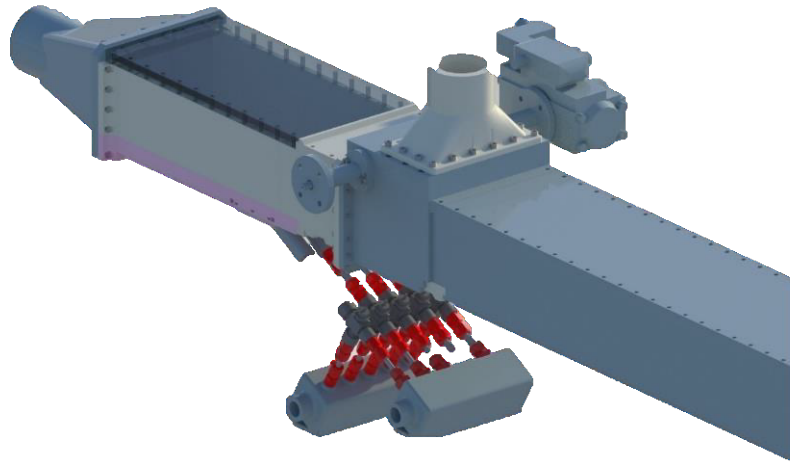


Figure 4.1: TLCs Rig

Flow Visualization

For the flow visualization, as at the time the exact type of test that will be performed was unknown¹, it was deemed necessary to have top and side access for the infrared camera. The access was achieved by using non coated sapphire windows. Although better IR materials could be used, as the experiment was focused in flow visualization rather than in quantitative measurements, the lower transmission of 85% did not affect the results in a significant matter.

Regarding manufacturing, the test rig was printed in PA12, using Selective Laser Sintering (SLS).

¹See different methods in section 4.2

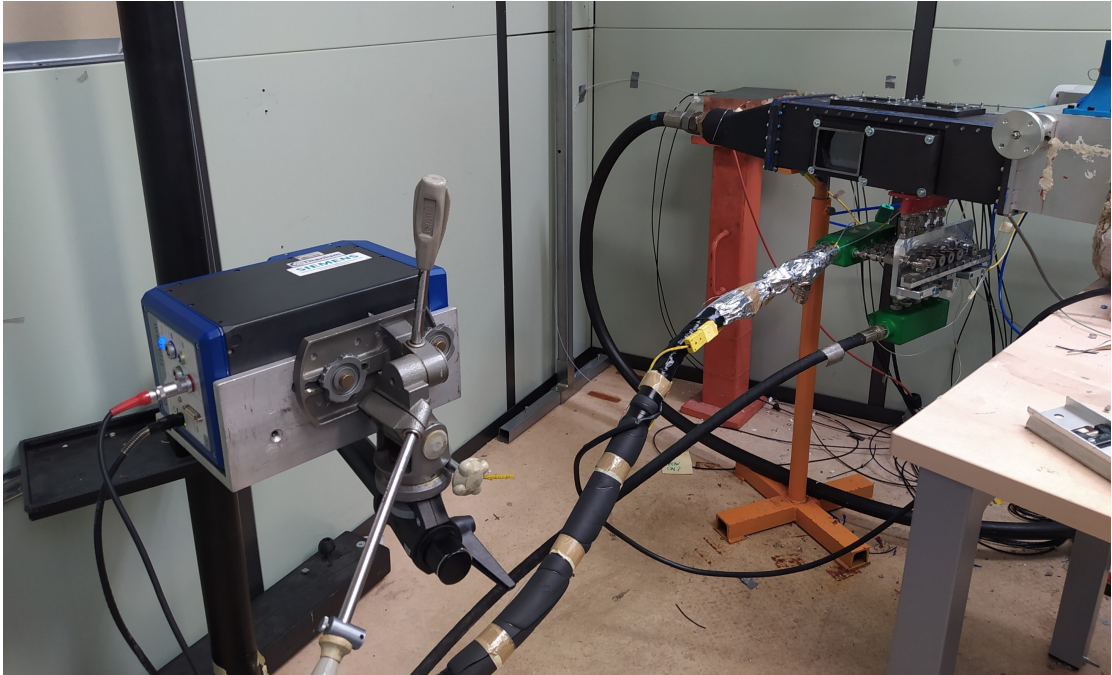


Figure 4.2: Test Set-up

As seen in the Figure 4.1, the side window slots are positioned so that the edge of the inside frame is flushed with the floor of the rig. As for "blank windows", used to cover the remaining slots, acrylic windows were available in case optical access was needed.

The red component seen attached to the base of the test rig is the coolant port. Either a film-cooling test object or a holder for porous geometries was mounted (Figure 4.3).

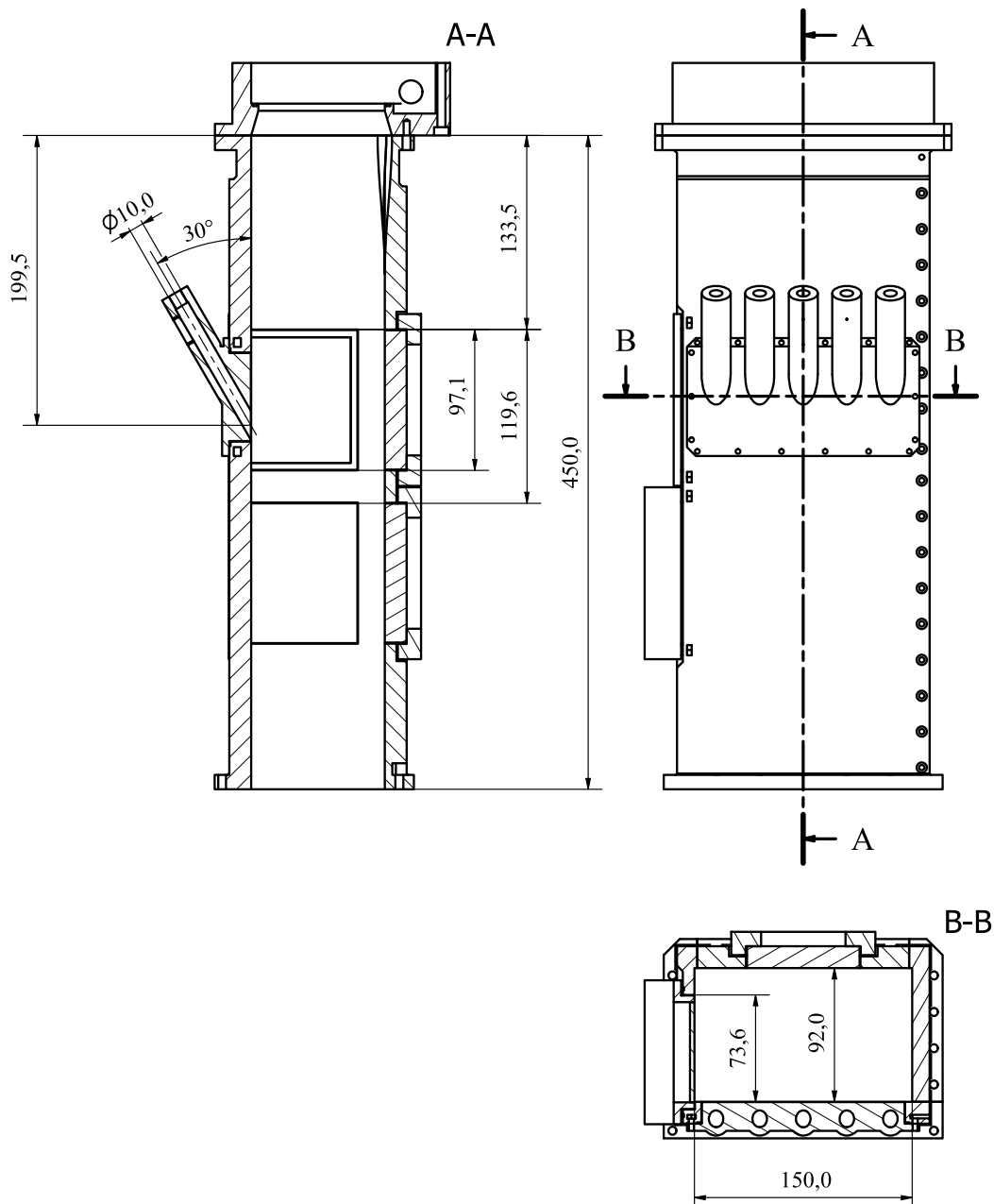
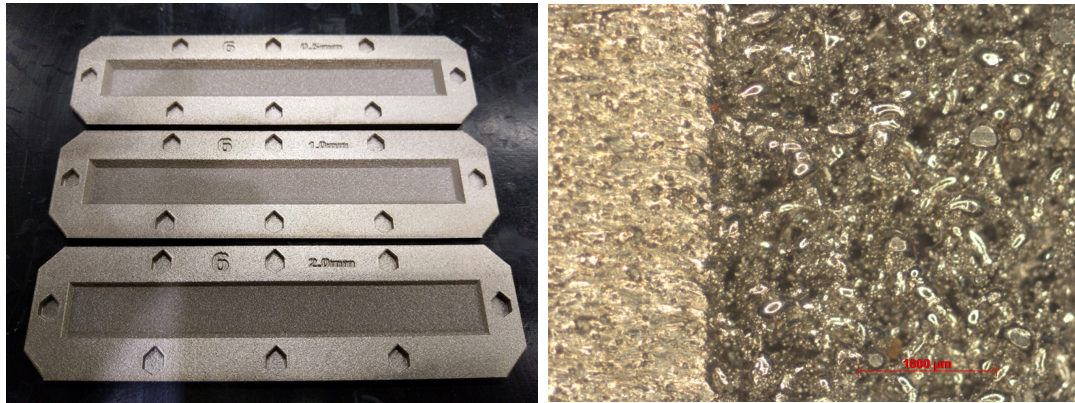


Figure 4.3: Section view of test rig with film-cooling test objects attached

4.1.2 Test Samples

Porous test objects were manufactured in Hastelloy-X (Batch 2019) and Inconel 625 (Batch 2020)². They were manufactured using Laser Powdered Bed Fusion. As observed in Figure 4.4a, the samples are made by placing a porous strip surrounded by a solid metal frame³.



(a) Test Objects with Different Thickness (b) Detail of Test Object Surface
Figure 4.4: Images of the Test Objects and Detailed View of the Surface

As seen in Figure 4.4b, the porous present in the sample are defects in the structure where the material was not molten by the laser. This un-molten pockets were filled with metal powder during the printing process that was removed when cleaning the test object.

4.1.3 Instruments and data collection

Temperature, mass-flow and pressure sensors

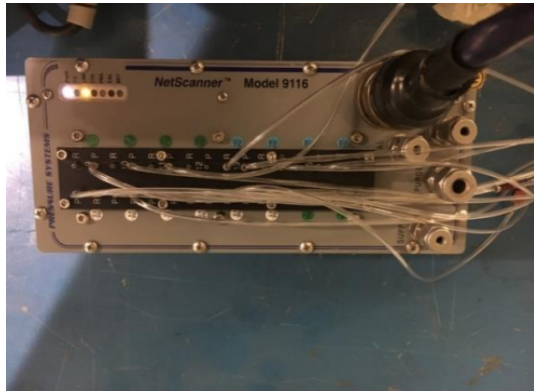
Relative pressures were recorded using a *NetScanner Model 9116* (Figure 4.5a). This device has 16 piezoresistive pressure sensor channels able to resist values in the range of 1 - 690 kPa. It achieves this by using sensors whose maximum detectable pressure is 1, 5, 15 and 100 psi⁴.

Ambient pressure was measured by a *Rosemount 2088 Gage and Absolute Pressure Transmitter* (Figure 4.5b).

²Chemical composition of the materials is included in Table 6.10

³Technical drawing in Appendix C

⁴6.9, 34.5, 103.5 and 690 kPa respectively



(a) NetScanner Model 9116



(b) Rosemount 2088

Temperatures and other voltage dependent measurements were recorded using a *Datascan 7220* 16 channel measurement processor (Figure 4.6). Type K thermocouples were mainly used for the temperature measurements.

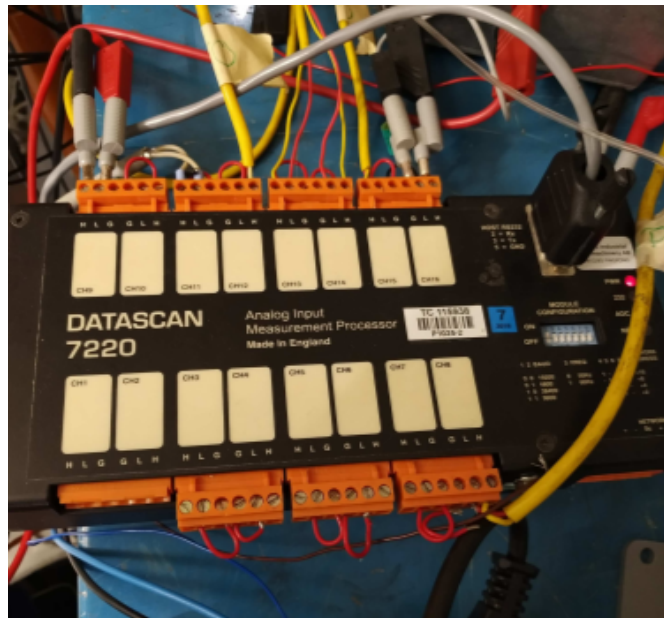


Figure 4.6: Datascan 7220 16 channel measurement processor

Main flow mass-flow was measured using a orifice plate, while coolant flow mass-flow was measured using a SITRANS FC MASS 2100 coriolis flow-meter (Figure 4.7).



Figure 4.7: SITRANS FC MASS 2100

In order to process and collect the data from all the measurement devices, Rigview, an in-house developed software programmed on LabView was used.

IR Camera

Infrared recordings were captured using a *CEDIP Titanium 560M* camera (Figure 4.8). It has an InSb sensor of 640 x 512 pixels, with a spectral response in the range 3.6 - 5.1 μ m.



Figure 4.8: Titanium 560M

4.2 Procedure

As mentioned in Section 3.3.3, even though it is technically possible to get quantitative measurements of gas concentration, in most of the cases this may be too complicated or even impossible.

Because of the requirements of this experiment, it is not possible to have the objects that may induce scattering far from the CO_2 injection place. As a result, it is only possible to get qualitative results.

Two main procedures for CO_2 injection are presented:

- Main flow injection: CO_2 is injected using a small injector in the main flow, with the aim to generate a streamline
- Coolant flow injection: CO_2 is used as a coolant and recorded from the side, with the aim to obtain its coverage

It is recommended to have some feature easily distinguishable in the background to aid with the camera focusing. As the background is black painted, a small strip of metal tape outside the region of interest could be used.

4.2.1 Main Flow Injection

For this methodology, CO_2 is injected upstream of the measuring region using a small injector. The injected CO_2 will then, if injected at the correct pressure⁵, follow the flow and generate a streamline that can be recorded with the IR camera.

As multiple viewing angles are needed in order to assess the three dimensional form of the streamline (if the flow is not approximately two dimensional), different recordings must be taken or, ideally, a set-up with multiple cameras should be used.

As in order to get a clear signal from the flow background subtraction must be used, a clean plate of the background must be taken. Moreover, to properly detect the CO_2 this has to be injected at a different temperature from its surroundings (the higher it is, the higher contrast it will be obtained). As discussed in Section ??, it is possible to use a cold or hot injection depending on what is easier to use.

Using this methodology, it was considered easier to inject cold CO_2 with a heated background. Even though a mat heater could have been used as a heated background, it was decided to use heated main flow to heat the walls of the tunnel and detect the CO_2 using the scattering that it will be produced.

The main reason of this selection was that, as the flow needs to be recorded from different directions (side, top and at different angles between those) and a clean plate of the background must be taken it was considered acceptable considering

⁵If the pressure is too high, it will disturb the flow. If is too low, it will not be possible to have a consistent streamline

that custom made mat heaters for the floor of the tunnel with metal spreaders should be used in order to get a proper heated background at all times.

4.2.2 Coolant Flow Injection

For this methodology, CO_2 is injected through the tested sample. Even though it is possible to inject a non 100% concentration of CO_2 as coolant, it was decided not to do this to have better contrast and because it was easier to use. As the dimensional analysis of the experiment (Section 3.1) results in that the important parameters for the study are the Reynolds number of the main flow and the blowing ratio, if these are maintained with respect to the previous studies on heat transfer and cooling effectiveness, the obtained results will be comparable.

In order to detect the CO_2 , different methods can be used. It is possible to use the same technique as in the main flow injection, using heated main flow to heat the background and use the scattering. As this time the carbon dioxide is being recorded against the wall, it is possible to place a mat heater to increase the contrast with the background. Doing this, allows to run a ambient temperature main flow and CO_2 , having a more constant signal because the temperature of the carbon dioxide is not changing through the length of the experiment.

The steps to follow to run the experiment are:

1. Position the camera
2. Start the experiment using air as coolant until the background is stabilized
3. Switch coolant to carbon dioxide and wait until the background is stabilized
4. Start recording
5. Wait for 5s to obtain the CO_2 plate
6. Switch the coolant to air and wait until no CO_2 can be seen in the recording
7. Wait for 5 seconds to obtain the clean plate
8. Stop the recording

4.3 Post-Processing

As this experiment is a labor and data-intensive process, requiring multiple recordings, the process has been subdivided in different steps for which different automatic or semi-automatic post-processing steps have been developed.

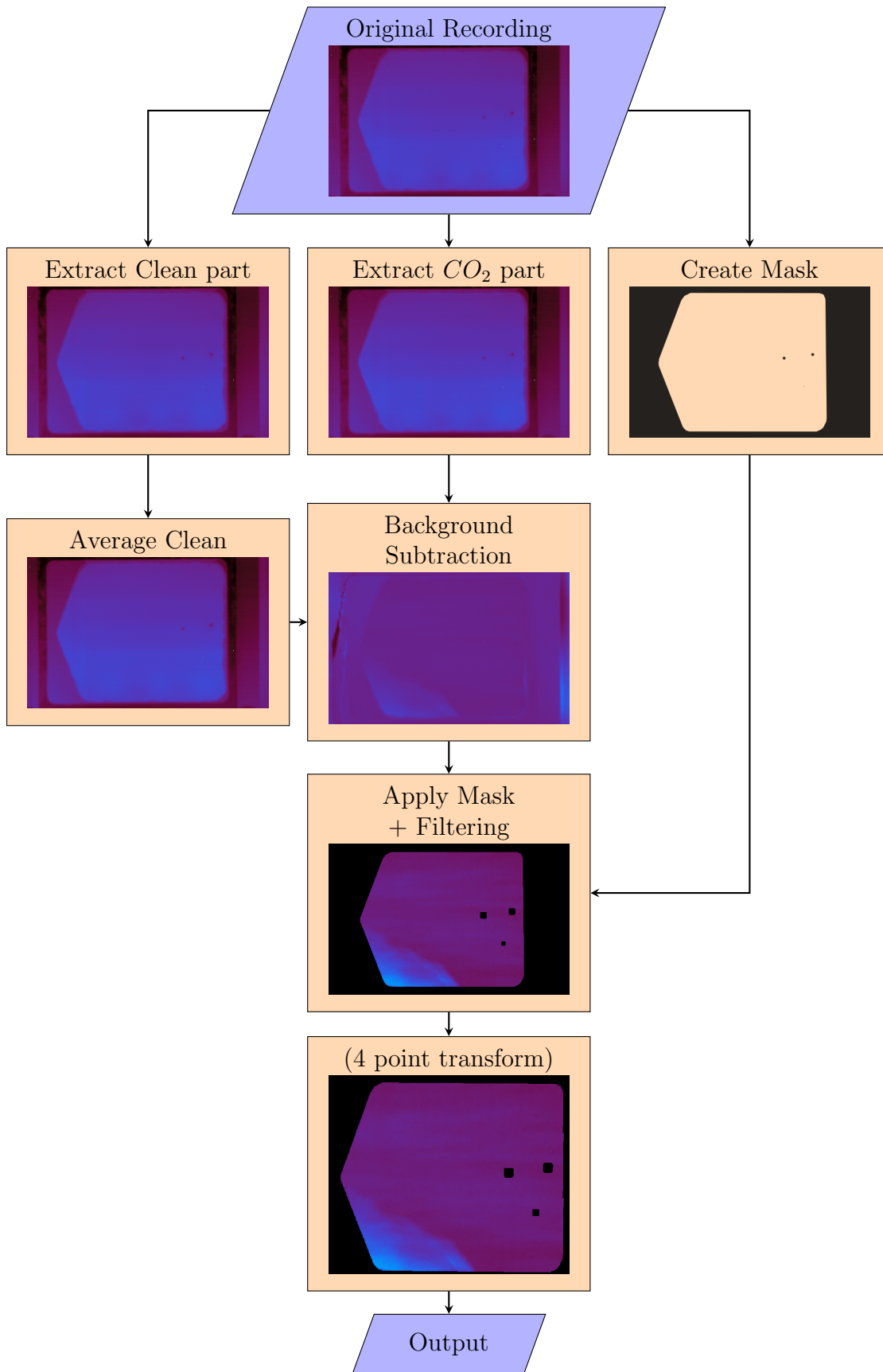


Figure 4.9: Post-processing flow diagram

The post-processing scheme can be seen in Figure 4.9. Optional steps are written between parentheses.

As it is difficult to get the exact point at which CO_2 stops flowing into the test rig when the coolant is switched to air, because it depends on the mass-flow injected, it was decided to record the whole experiment and then extract the part relative to the CO_2 and the part relative to air manually.

A mask is generated using a image editing software⁶. The mask consists on a PNG image where the part that the operator wants to be removed is not transparent.

As can be seen in the steps 1.1 and 1.2, no noticeable difference is distinguished between the part of the recording with CO_2 and without it because the signal is quite faint. An average clean plate is obtained in order to reduce background noise and a background subtraction is performed to reveal the flow.

As a background subtraction, the following formula is used:

$$result = \log \left(\frac{CO_2 \text{ plate counts}}{clean \text{ plate counts}} \right) \quad (4.1)$$

This formula is used rather than the conventional background subtraction because, in case there is no scattering from close hot objects, it is proportional to the concentration of the CO_2 . Also, this formulation is almost equivalent to the conventional background subtraction (Appendix D.1).

After this step, the mask is applied to highlight the region of interest and a Gaussian filter is applied.

The last step consists of applying a 4 point transformation to correct any small rotation / deformation on the window due to the positioning of the camera. This step is optional as in some cases it is desired to record the flow at an angle. An example of this will be main flow CO_2 injection (Section 4.2.1).

Additional post-processing steps such as convolution kernels to highlight edges, sharpen the image, etc, or coolant isolation using a threshold may also be used.

⁶GIMP was used, but any program may be used

Chapter 5

Results and Discussion

5.1 Main Flow Injection

(a) $h = 2 \text{ mm}$

(b) $h = 5 \text{ mm}$

(c) $h = 7 \text{ mm}$

(d) $h = 10 \text{ mm}$

(e) $h = 15 \text{ mm}$

(f) $h = 20 \text{ mm}$

Figure 5.1: Main Flow Injection at different heights, B19-P1-1.0mm BR = 1.0

The images shown in Figure 5.1 have been obtained by extracting the tracer from the image using a threshold and overlaying it over a generated background.

As a remark, a different test rig side panel was used for this tests, were the side windows were not flush with the floor.

As seen in Figure 5.1, the obtained result is similar to injecting smoke in the flow. The tracer properly follows the flow and highlights where the film-layer is present. However, special care has to be taken to not inject at a excessive pressure.

Although main flow injection generated streamlines successfully, the dimension of the flow details that were to be measured were to small for this technique. For this reason, this method was not used to get final results.

5.2 Coolant Flow Injection

5.2.1 Heated Flow, Cold CO_2

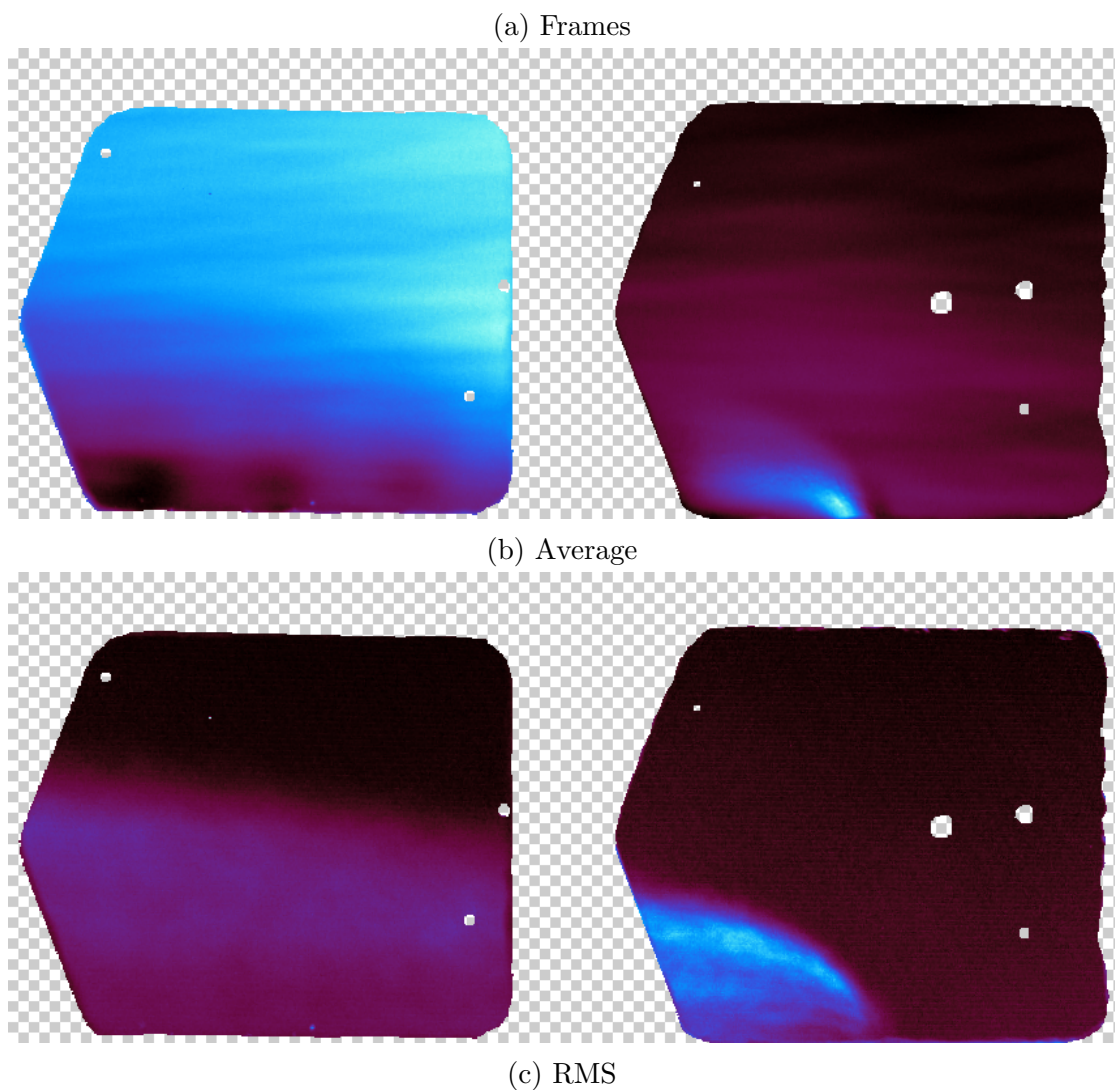


Figure 5.2: B20-P1-1.0mm M=1.0 cold CO_2

When injecting carbon dioxide at ambient temperature and having the flow at higher temperature, the lengthwise change in CO_2 temperature alters the results.

In this recording conditions, the main detection method is absorption from the back plate, but it exists some scattering from the front plate. Nevertheless, this will generate a constant signal. The problem comes from the change in temperature of the carbon dioxide, as it causes it to absorb less radiation from the background and changes its behaviour (Figure 3.6).

This change makes hard to recognize if the resulting change of signal is due to flow conditions or the temperature change of the CO_2 , as it is possible to get zero signal in a region of the image.

5.2.2 Heated Flow, Hot CO_2

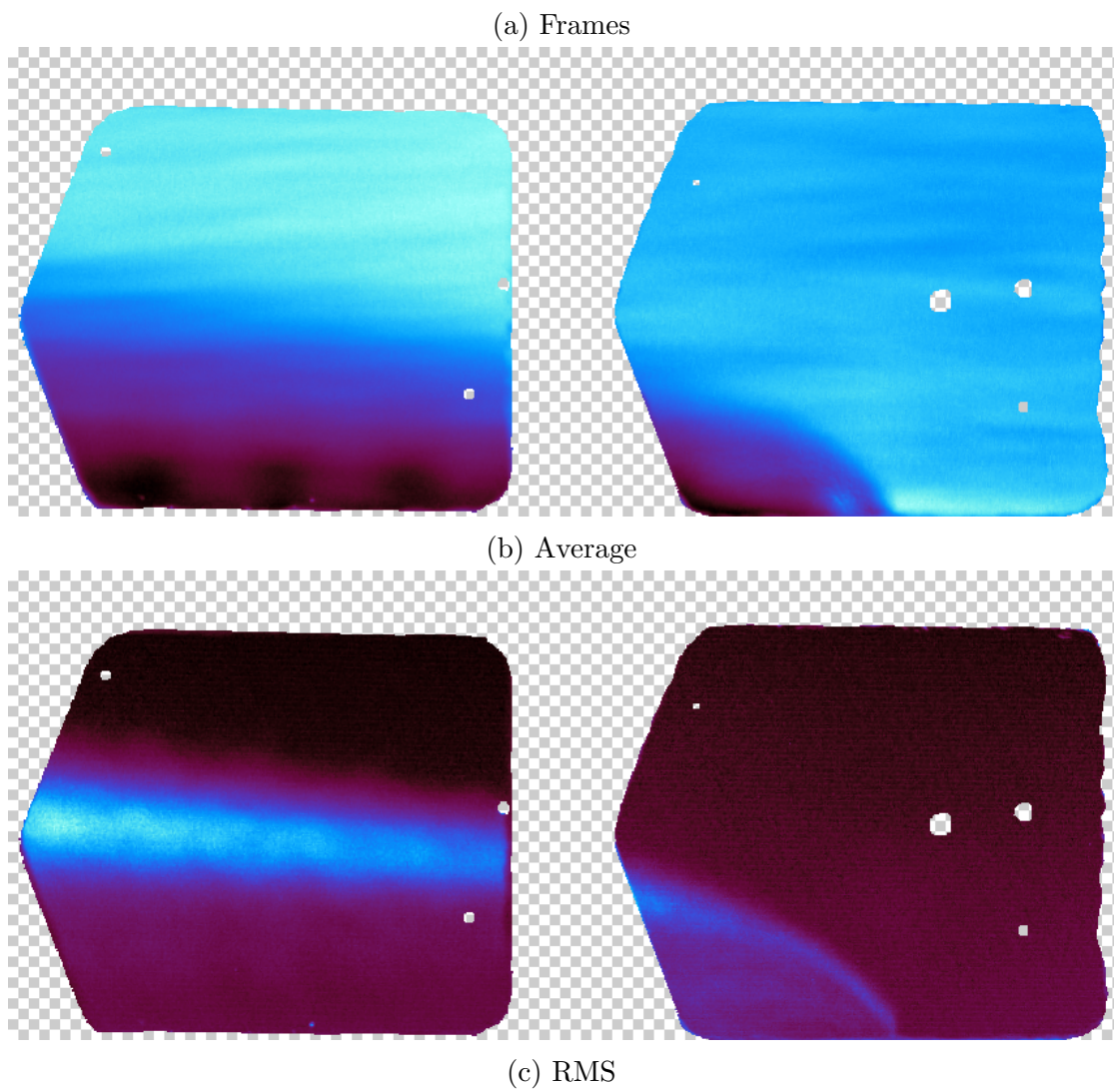


Figure 5.3: B20-P1-1.0mm $M=1.0$ hot CO_2

Although, theoretically, when injecting hot carbon dioxide the resulting signal should be fainter, it achieves better signal characteristics.

As the varying signal effect due to the change in temperature is removed, the obtained pictures present a more uniform view of the flow. Comparing between the average pictures (Figure 5.2 and 5.3), it is clearly seen how in the latter case the signal shows as negative all the time, rather than changing from positive to negative between windows.

This makes it easier to get the boundary between the film layer and main flow.

5.2.3 Heated Background

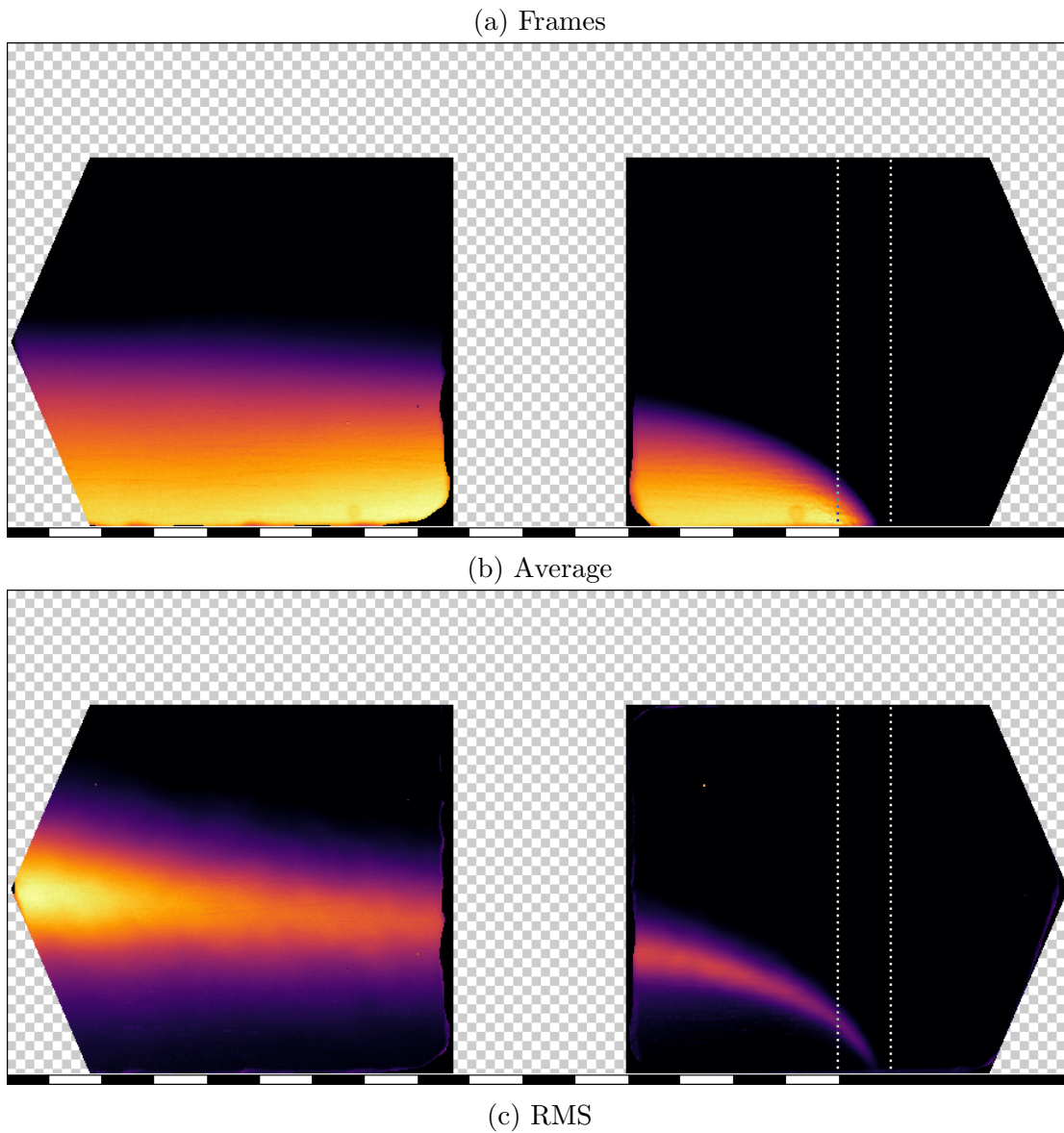


Figure 5.4: B19-P1-0.5mm M=1.0 heated background

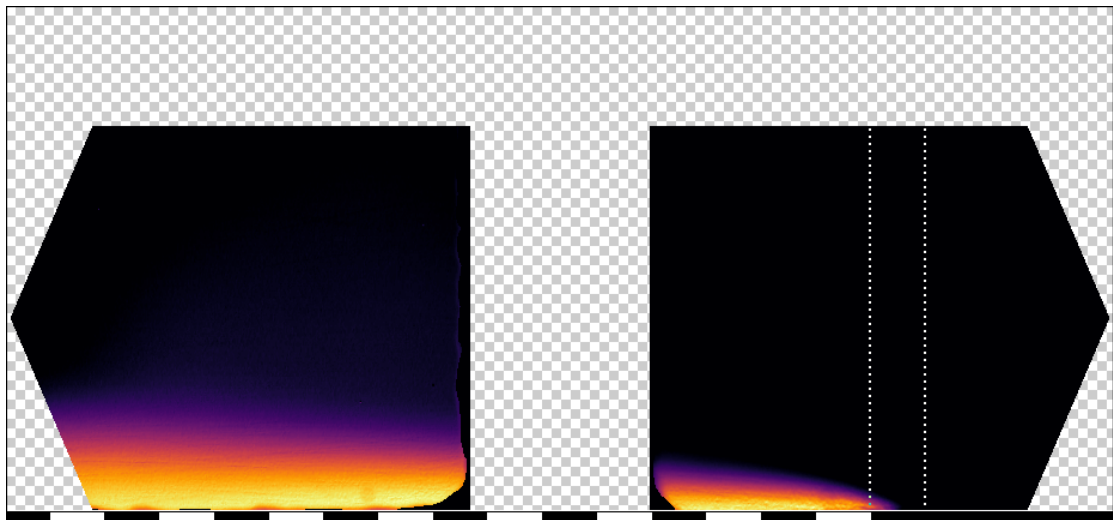
As a side note, the rectangles shown at the bottom of the results represent the adimensional length downstream. One rectangle represents one sample length.

As when injecting hot carbon dioxide, a heated background achieves better results because the dependency between signal strength and temperature is removed.

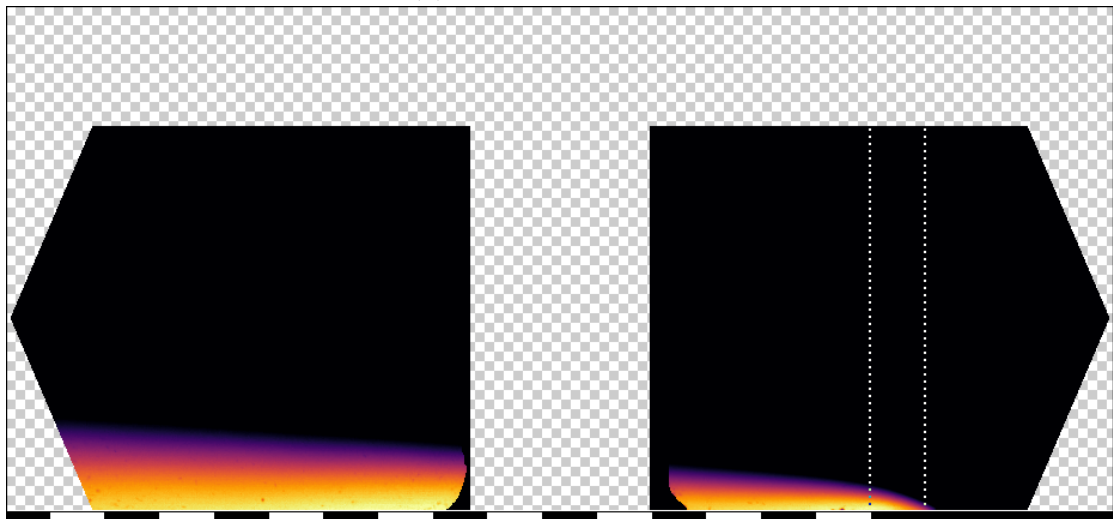
However, this achieves better results than the latter one. The main explanations for this is that a high temperature difference can be achieved between the carbon dioxide and the background emitter.

As a summary, good flow visualization can be achieved using the “heated flow and seeder” technique and “heated background”. However, the second one achieves better results so it is the recommended one to use if possible. As a heater and heat spreader has to be placed on the background, it may be difficult to implement in situations where the background is not flat.

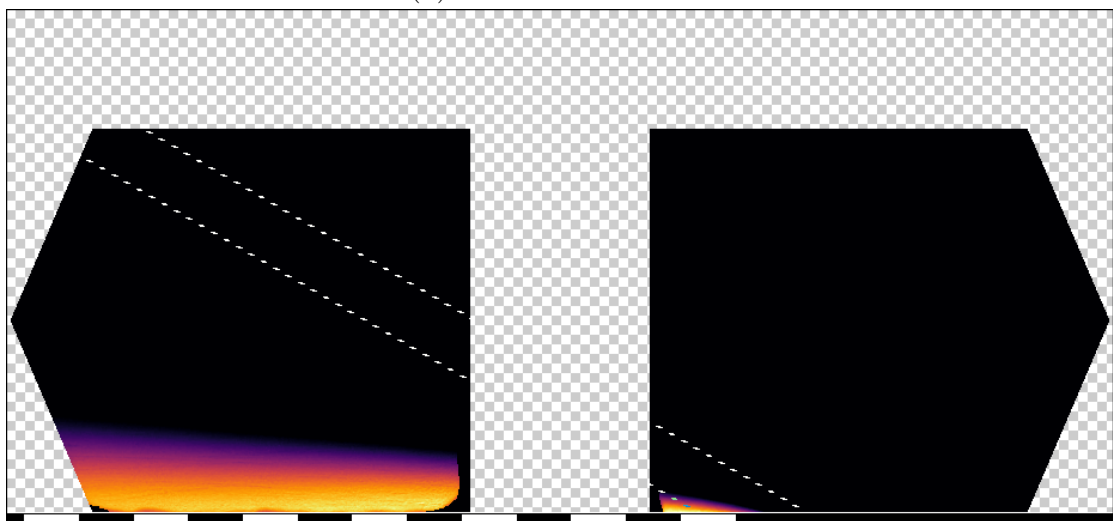
5.3 Sample Comparison



(a) thickness = 0.5 mm

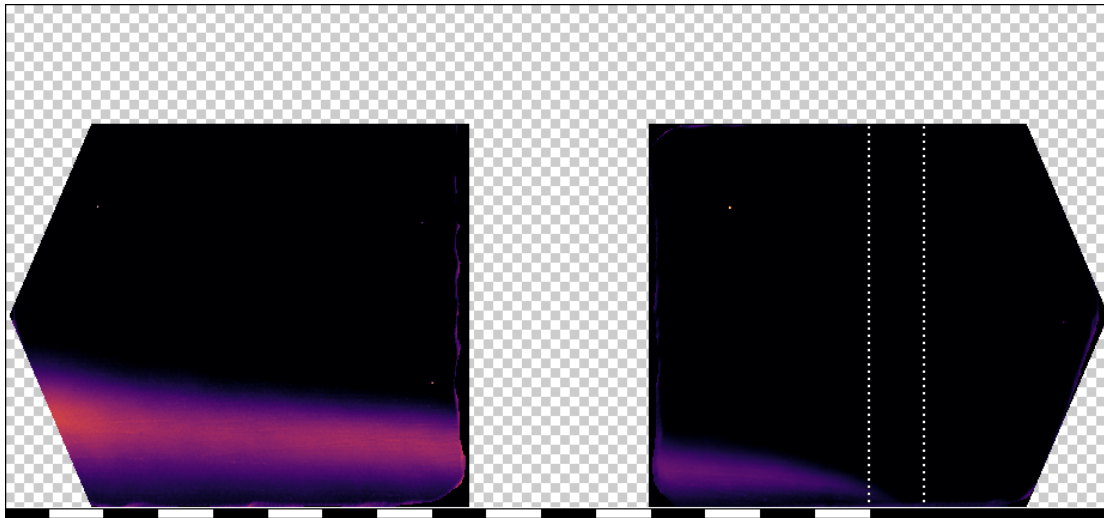


(b) thickness = 2.0 mm

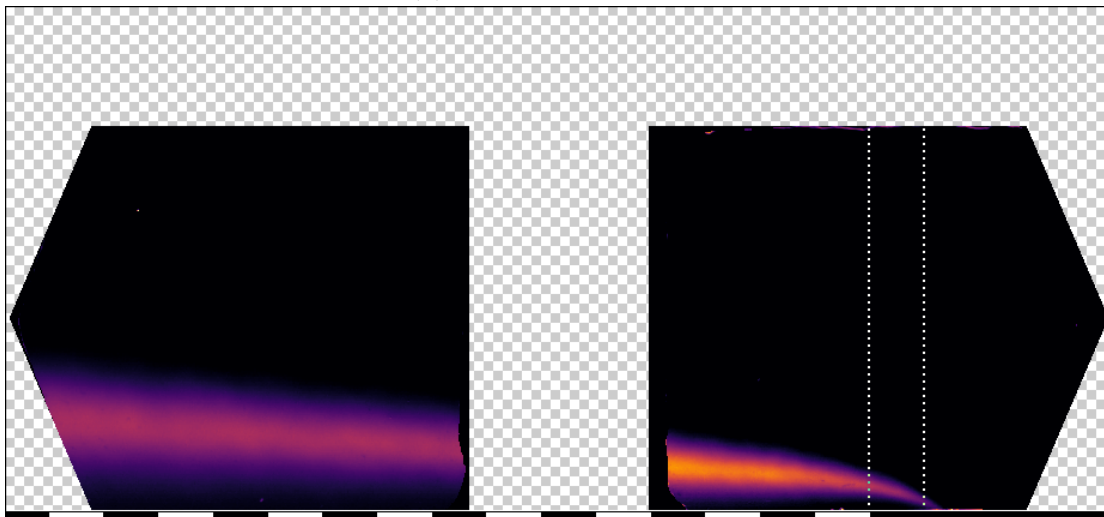


(c) filmcooling

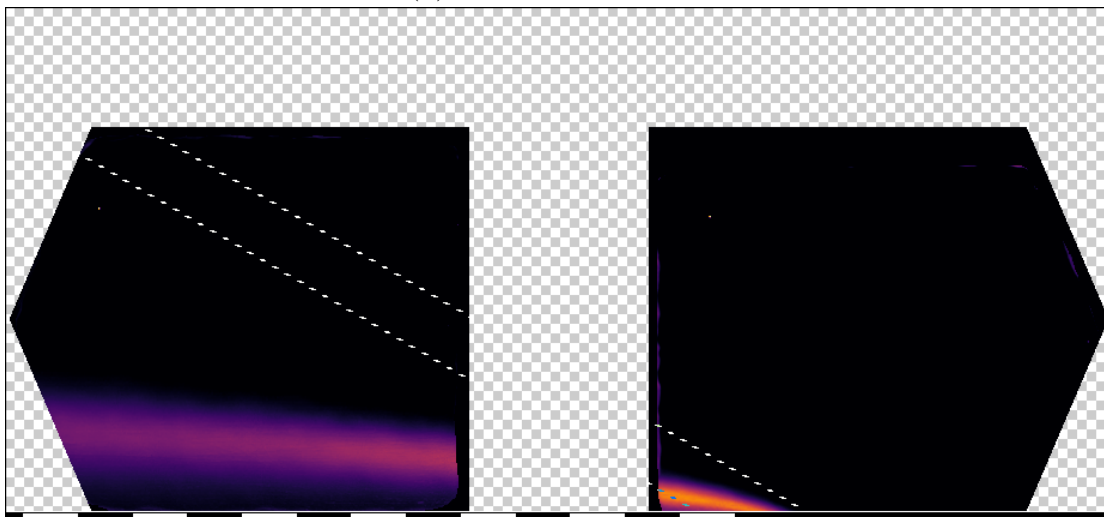
Javier Soriano Lluch Figure 5.5: AVG, Blowing ratio = 0.5



(a) thickness = 0.5 mm



(b) thickness = 2.0 mm



(c) filmcooling

Figure 5.6: RMS, Blowing ratio = 0.5

In Figure 5.5 it is displayed the averaged absorbed radiance. No units have been used, as the aim of the results is to show qualitative results. However, the colorbar has the same limits in all the results to be able to compare them¹.

Regarding the sample with thickness 1 mm, the injection appeared to start before the porous part of the test object. The most probable cause of this strange result is a CO_2 leak at the interface between the sample and its holder. For this reason, this sample will be not commented further as the flow conditions will differ between the heat transfer and flow visualization results.

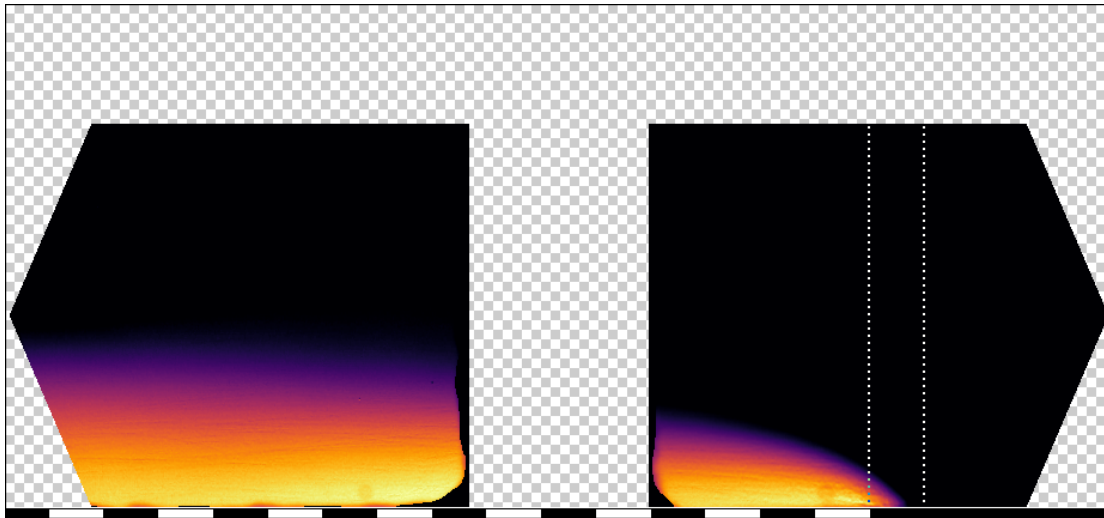
On the contrary, the samples with thickness 0.5 mm and 2.0 mm have the injection situated between the boundary lines. This indicates that there was no leak upstream of the injection points.

Comparing 0.5 mm and 2.0 mm, the former does not show carbon dioxide in all the region. Previous water testing studies performed on the test object show uniform jets through the sample [13]. This difference may be caused by the different pressure drop that exist between the samples. As the sample with thickness 0.5 mm is injected at a lower pressure, the main flow could be blocking the channels.

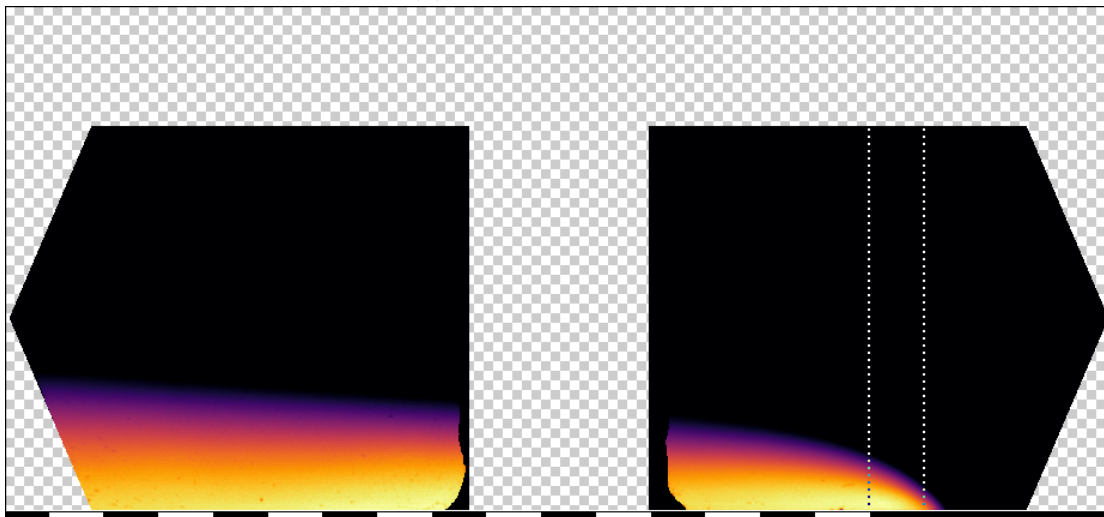
Looking at the RMS (Figure 5.6), it is seen that the test object with thickness 2.0 mm presents higher turbulence intensity. However, the width of the mixing layer seems to be thicker for 0.5 mm.

Regarding the filmcooling test object, although it is injected at a 30° angle, it has a similar mixing layer height compared to the transpiration cooling samples. Moreover, regarding the RMS, its values are comparable to the 2.0 mm sample.

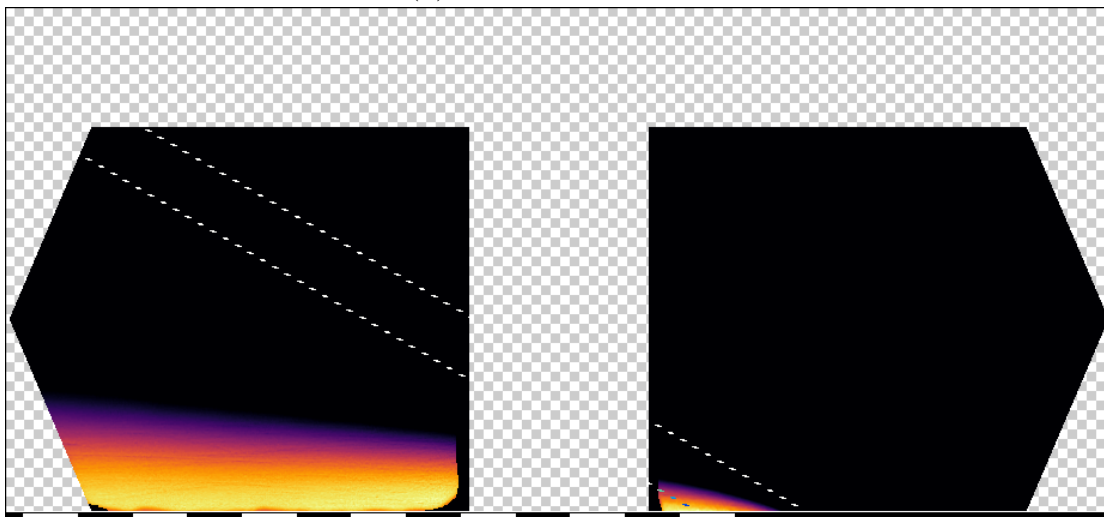
¹Different limits have been used for AVG and RMS



(a) thickness = 0.5 mm

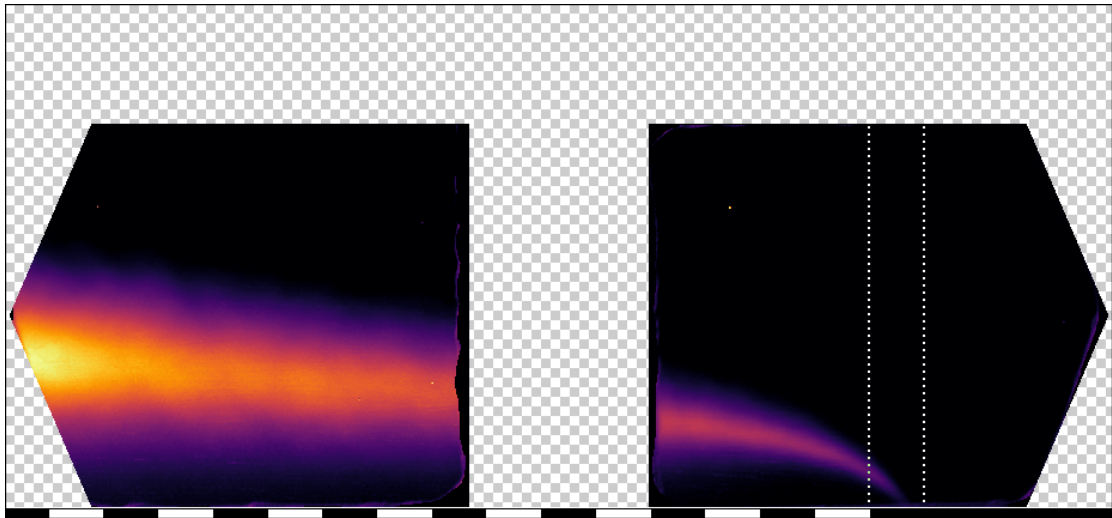


(b) thickness = 2.0 mm

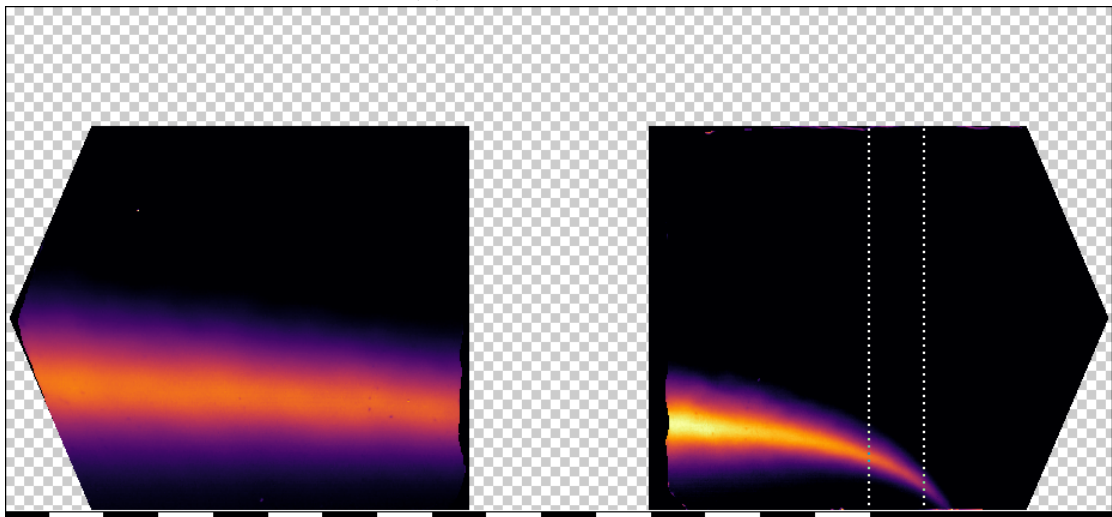


(c) filmcooling

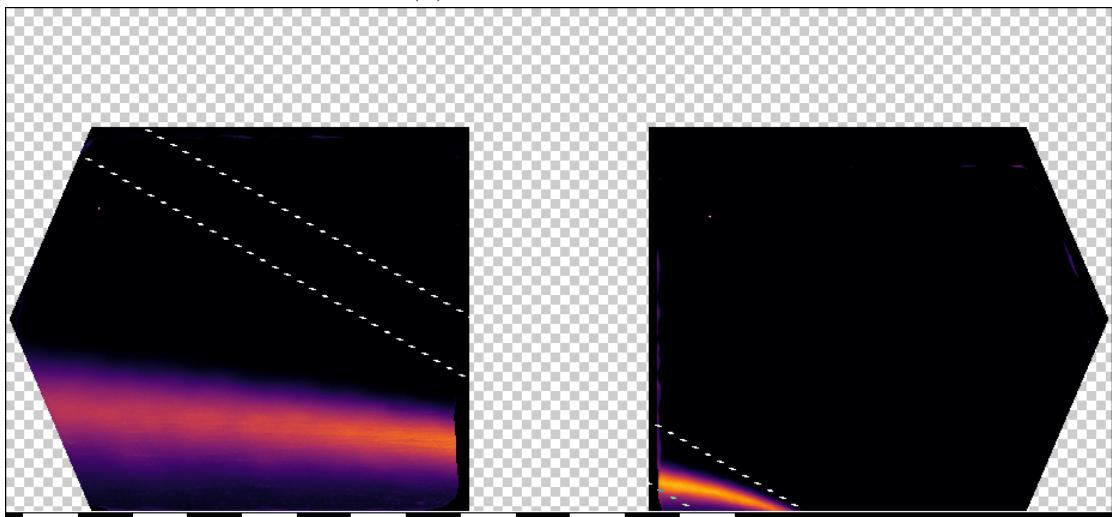
Figure 5.7: AVG, Blowing ratio = 1.0



(a) thickness = 0.5 mm



(b) thickness = 2.0 mm



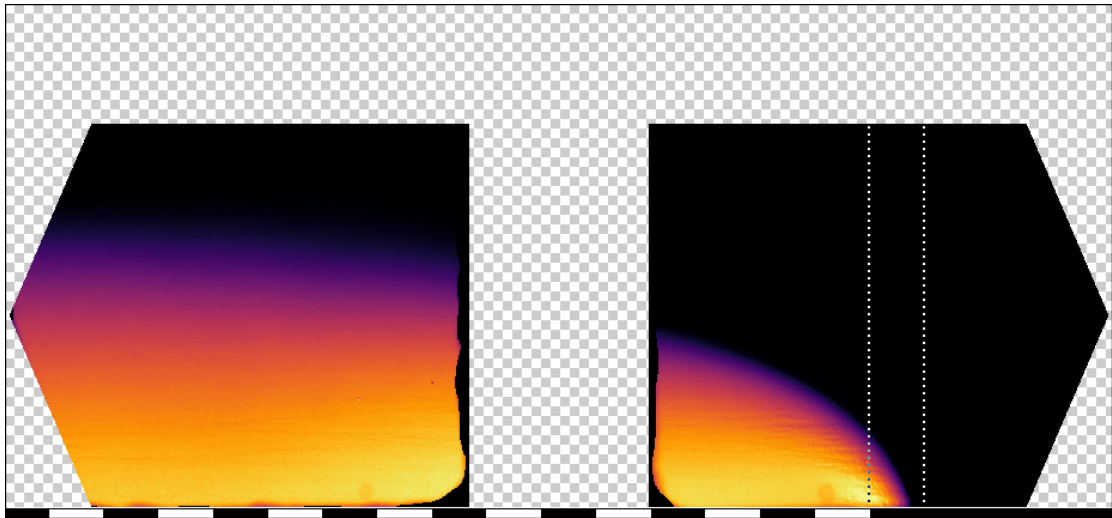
(c) filmcooling

Figure 5.8: RMS, Blowing ratio = 1.0

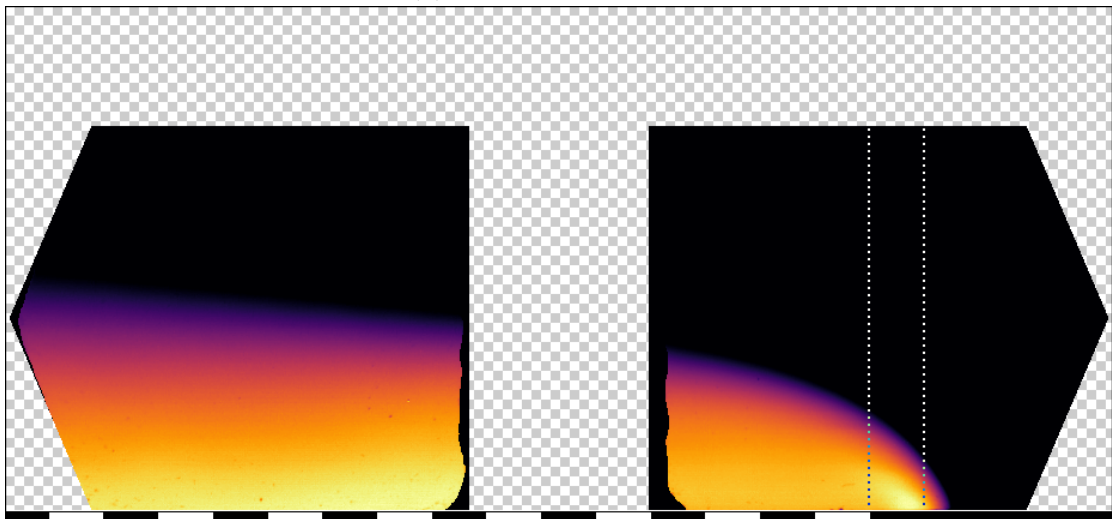
Regarding samples 0.5 and 2.0 mm (Figure 5.5), the thinner sample presents a higher coolant layer than the thicker one. Also, comparing the results with $BR = 0.5$, the start of the injection seems to have moved upstream. This can be explained by the coolant being fed at a higher pressure to achieve the higher blowing ratio.

Although the test object with thickness 2.0 mm has higher turbulence intensity in the upstream window, it is clear that in the downstream window 0.5 mm achieves higher values (Figure 5.8). As mentioned before, 0.5 mm presents a thicker mixing layer. Compared to the results at $BR = 0.5$, the turbulence intensity is significantly higher.

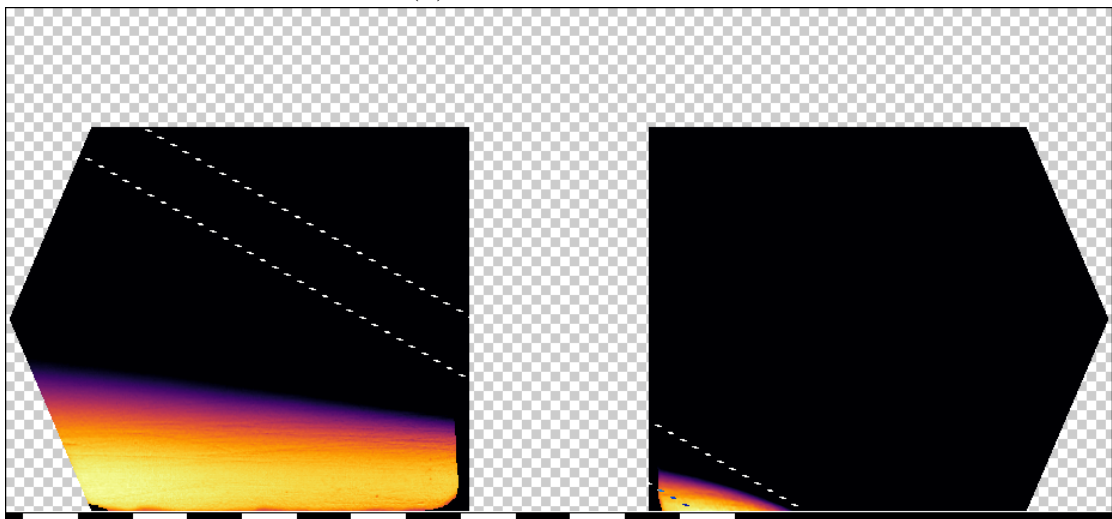
Regarding the filmcooling test object, this time it presents a lower mixing layer height compared to the transpiration cooling samples. Looking at the RMS, it is seen that the upstream window has similar maximum values, but in the downstream window they are slightly lower. However, in this case, the thickness of the mixing layer is substantially thinner.



(a) thickness = 0.5 mm

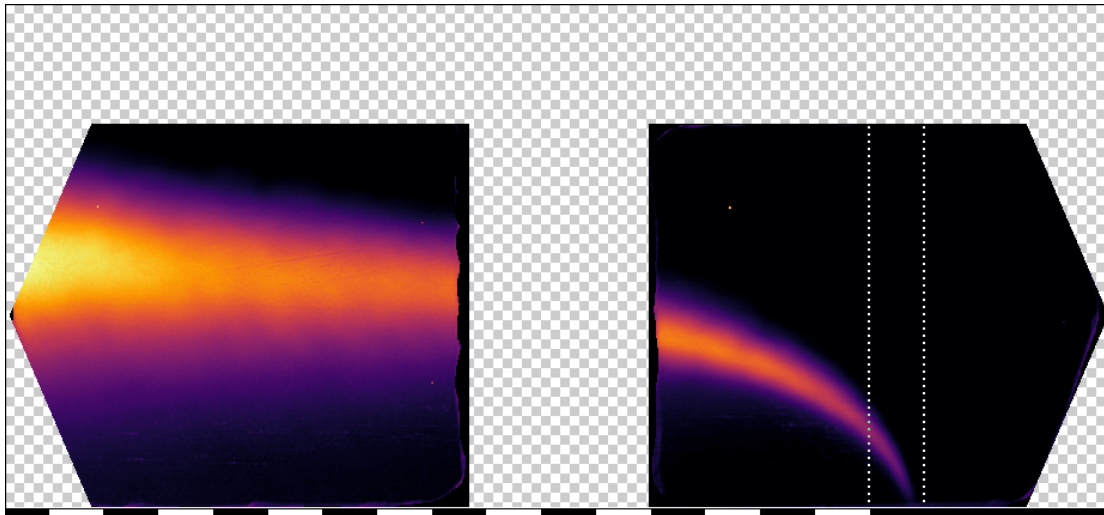


(b) thickness = 2.0 mm

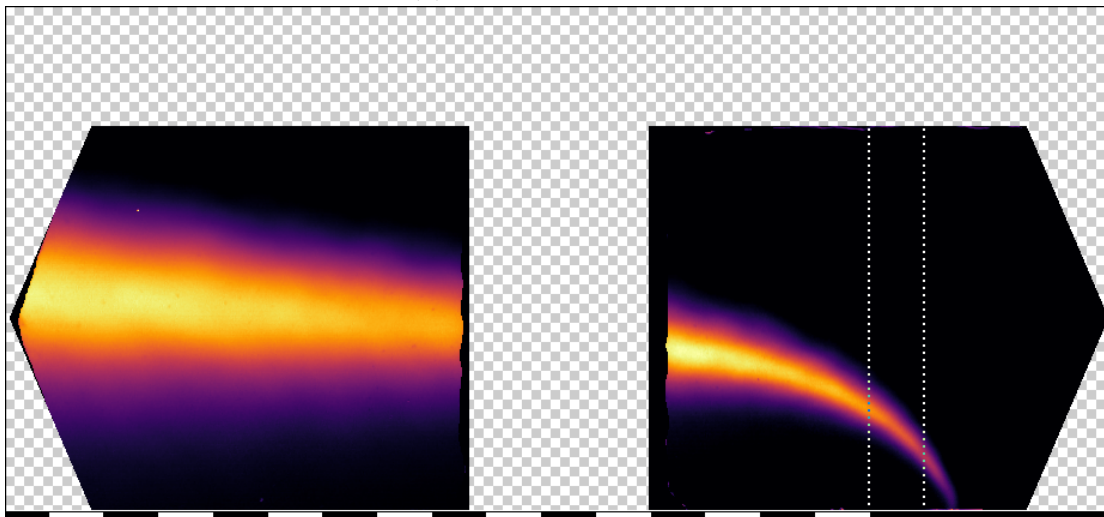


(c) filmcooling

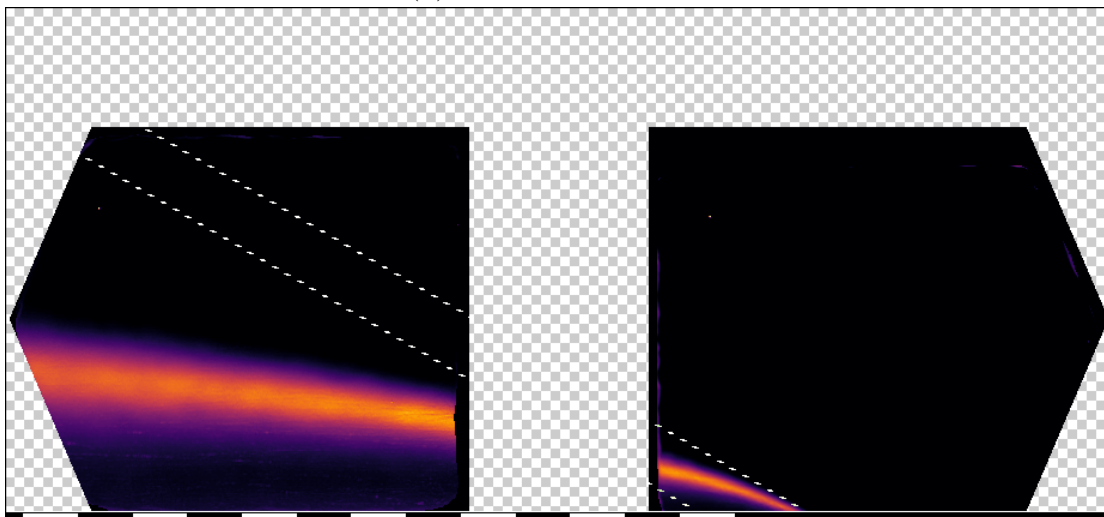
Figure 5.9: AVG, Blowing ratio = 2.0



(a) thickness = 0.5 mm



(b) thickness = 2.0 mm



(c) filmcooling

Figure 5.10: RMS, Blowing ratio = 2.0

Looking at Figure 5.9, the evolution is similar than the one present between Figure 5.5) and 5.7). The sample with thickness 0.5 mm does not fully cover the porous area. However, the injection start has advanced upstream.

Although in the upstream window the thicker sample has higher turbulence intensity, contrary to changing from $BR = 0.5$ to $BR = 1.0$, the 2.0 mm test object presents higher turbulence.

Regarding the filmcooling test object, as in $BR = 1.0$, it presents a significantly lower mixing layer height compared to the transpiration cooling samples. Looking at the RMS, it is significantly thinner.

As it is difficult to compare the height of the mixing layer by looking at the image results, this one will be obtained by taking the highest RMS value in the lengthwise coordinate (Figure 5.11).

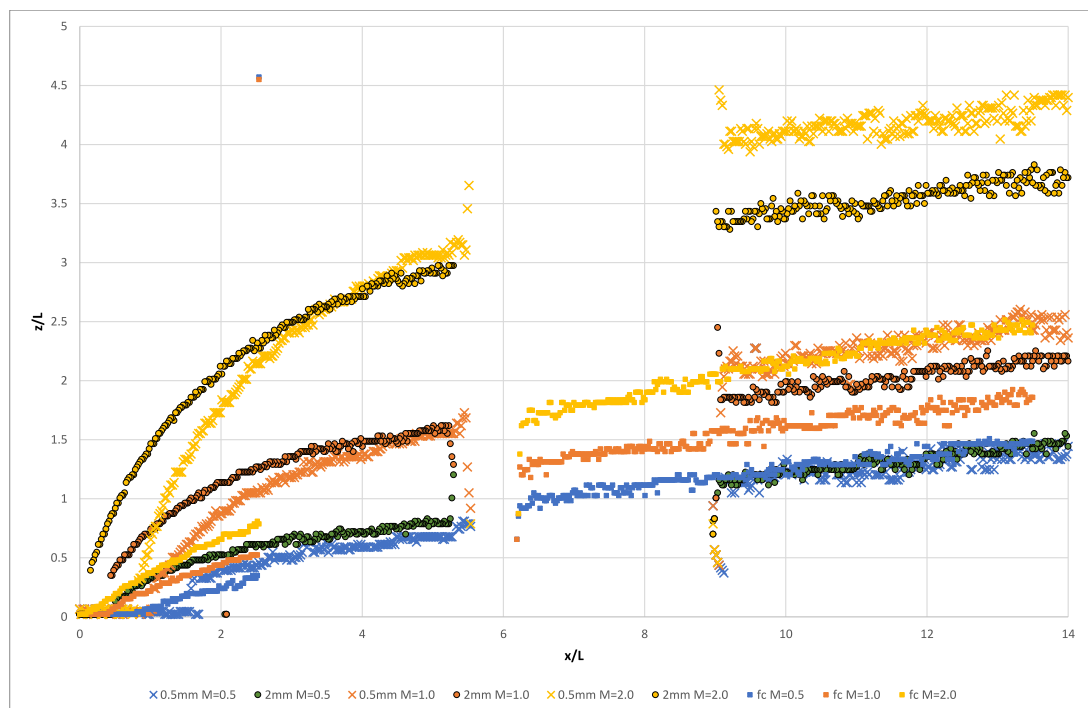


Figure 5.11: Mixing Layer Height

Regarding $BR = 0.5$, thickness 0.5 mm presents a lower heat transfer coefficient than 2.0 mm although the height of the mixing layer is lower for 0.5 mm. However, the turbulence intensity is higher for 2.0 mm, which should increase its heat transfer coefficient. For the downstream window, the heat transfer coefficient becomes more almost identical after $\xi_x = 8$. At this point, both test objects present similar RMS values and mixing layer height. Looking at the film-cooling sample, it presents similar heat transfer coefficient values. As it has a similar height, thickness and values for the mixing layer, this correlates with the heat transfer results.

Regarding $BR = 1.0$, thickness 0.5 mm presents a higher heat transfer coefficient than 2.0 mm. For the upstream window, as in last case, RMS is higher

for 2.0 mm but the mixing layer height is significantly lower for 0.5 mm. At the downstream window, the difference in heat transfer coefficient gets smaller with the lengthwise coordinate. In this case, the mixing layer height is higher for 0.5 mm, but also is its RMS. Looking at the film-cooling sample, it presents significantly lower heat transfer coefficient values. As it has a lower height, thickness and slightly lower values for the mixing layer, this correlates with the heat transfer results.

Regarding $BR = 2.0$, it follows a similar tendency to $BR = 1.0$ for the upstream window. However, at the downstream window, 2.0 mm presents both a higher RMS and lower mixing layer height. This correlates with its higher heat transfer coefficient. Looking at the film-cooling sample, it presents significantly lower heat transfer coefficient values. As it has a lower height, thickness and values for the mixing layer, this correlates with the heat transfer results.

No clear tendency has been observed between the flow visualization results and the cooling effectiveness (Figure 5.13)

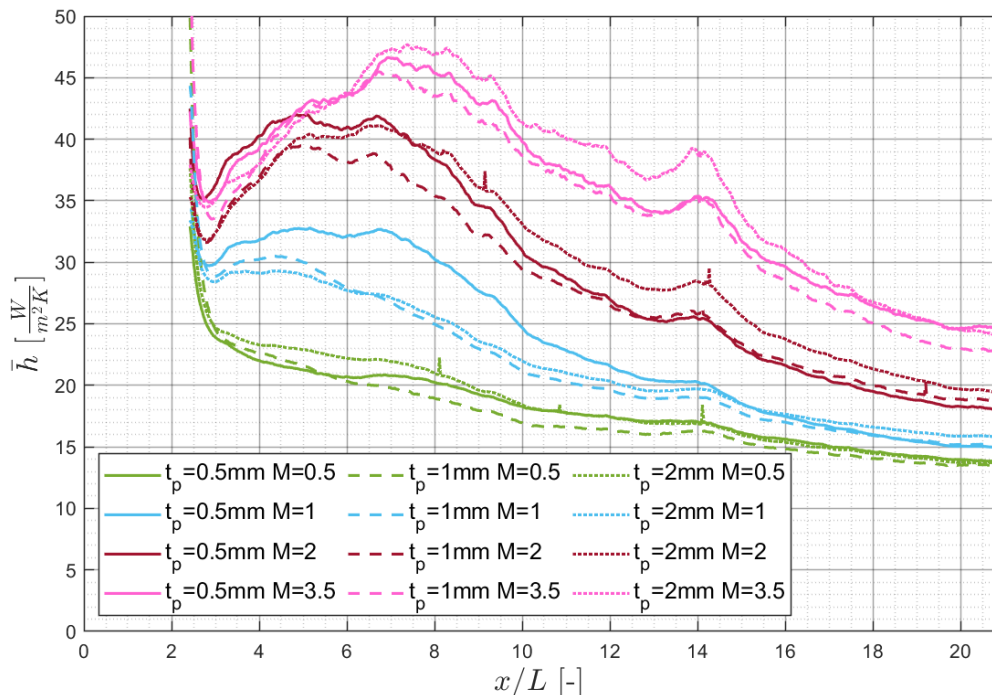
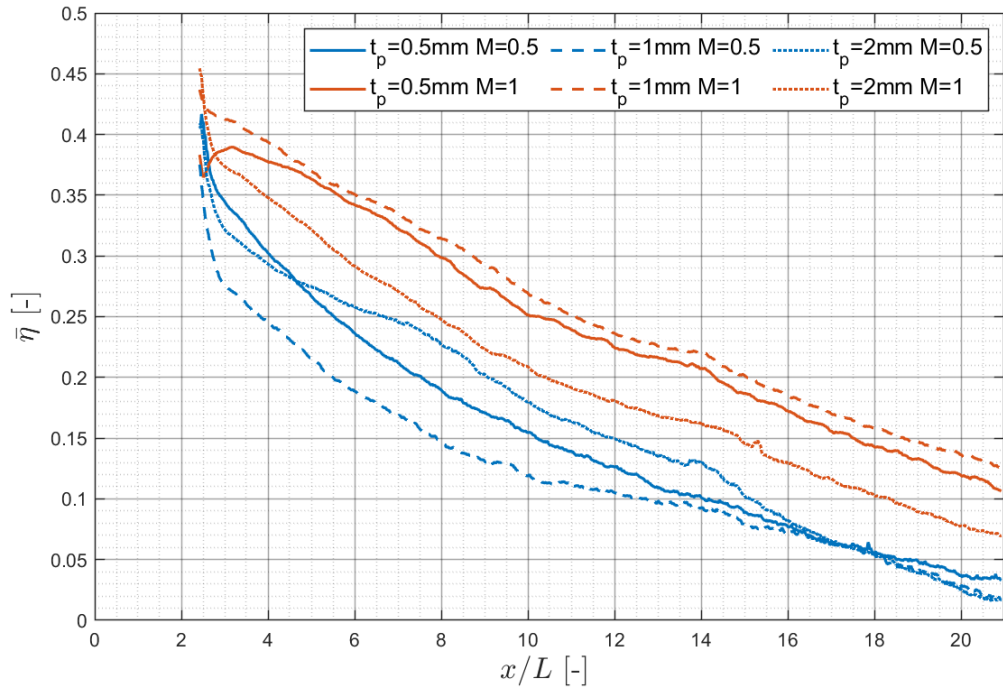
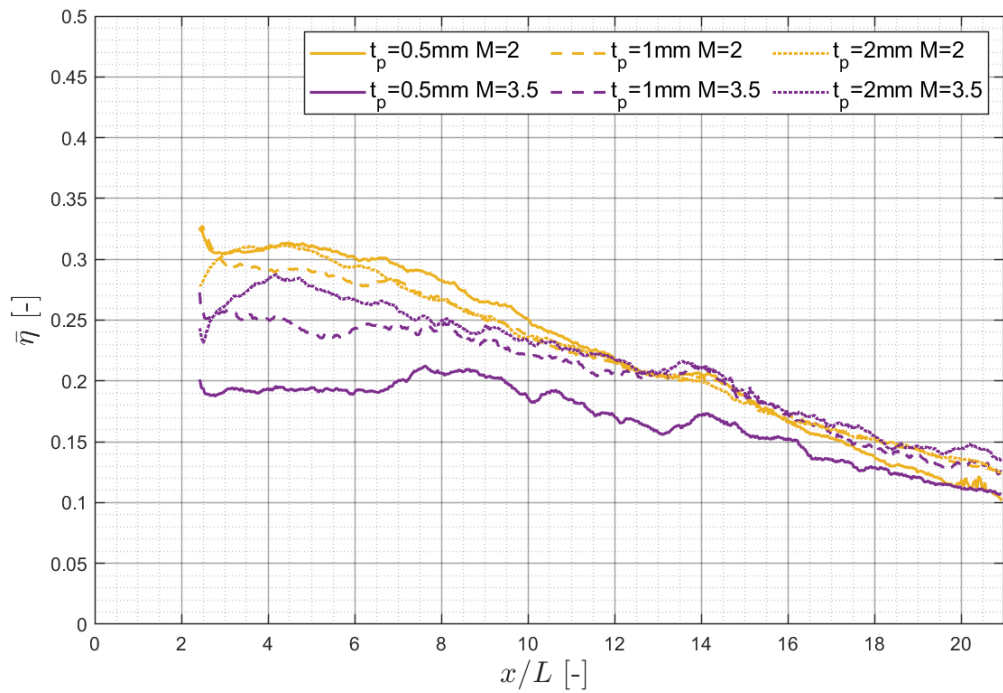


Figure 5.12: Lateral averaged heat transfer coefficient [13]



(a) BR = 0.5 and BR = 1.0



(b) BR = 2.0 and BR = 3.5

Figure 5.13: Laterally averaged blowing ratio [13]

Chapter 6

Conclusions

Following the study performed on flow visualization in transpiration cooling samples, the following conclusions are stated:

- Main flow injection produces significant results, but it was not possible to apply to the current experiment as the dimensions were too small.
- Between the different coolant injection techniques tested, using a heated background is the most recommended as it achieves the best results. However, as it may be difficult to implement, using a heated flow and heated carbon dioxide could be used. Cool flow and hot carbon dioxide is not recommended, as the signal received changes as the CO_2 heats up.
- As expected, the transpiration cooling samples have a higher mixing layer height due to the 90° injection angle.
- It is observed that the mixing layer height, thickness and RMS intensity affect the heat transfer coefficient. However, no clear difference between their magnitude could be observed.
- No clear correlation was observed between the flow visualization and the cooling effectiveness.

Bibliography

- [1] Electricity production by source — ourworldindata.org. <https://ourworldindata.org/grapher/electricity-prod-source-stacked>. [Accessed 27-Aug-2022].
- [2] Jet engine schematics. https://en.wikipedia.org/wiki/File:Jet_engine.svg, Jul 2014. [Accessed Aug-2022].
- [3] Brayton cycle - Wikipedia — en.wikipedia.org. https://en.wikipedia.org/wiki/Brayton_cycle. [Accessed Aug-2022].
- [4] Shailendra Naik. *Basic Aspects of Gas Turbine Heat Transfer*. 2017. ISBN 978-953-51-3093-2. doi: 10.5772/67323.
- [5] Ahmed F. El-Sayed. *Turbines*, pages 839–905. Springer London, London, 2016. ISBN 978-1-4471-6796-9. doi: 10.1007/978-1-4471-6796-9_10. URL https://doi.org/10.1007/978-1-4471-6796-9_10.
- [6] MATSUSHITA Laboratory. Thermal engineering laboratory. <https://www2.ashitech.ac.jp/mech/matsushita/TurbineCoolingen.html>.
- [7] Turbine cooling group, Nov 2017. URL <https://oti.eng.ox.ac.uk/research-groups/turbine-cooling-group/>.
- [8] BB-Agema femto engineering. Energy and utilities. <https://www.femto.eu/wp-content/uploads/2020/04/Siemens-SW-BB-AGEMA-Case-Study.pdf>.
- [9] Jacob C. Snyder and Karen A. Thole. Performance of Public Film Cooling Geometries Produced Through Additive Manufacturing. *Journal of Turbomachinery*, 142(5), 04 2020. ISSN 0889-504X. doi: 10.1115/1.4046488. URL <https://doi.org/10.1115/1.4046488>. 051009.
- [10] Markus Raffel. Background-oriented schlieren (bos) techniques. *Experiments in Fluids*, 56(3):60, Mar 2015. ISSN 1432-1114. doi: 10.1007/s00348-015-1927-5. URL <https://doi.org/10.1007/s00348-015-1927-5>.
- [11] M.D. Atkins and M.F. Boer. Chapter 2 - flow visualization. In Tongbeum Kim, Tian Jian Lu, and Seung Jin Song, editors, *Application of Thermo-Fluidic Measurement Techniques*, pages 15–59. Butterworth-Heinemann, 2016. ISBN 978-0-12-809731-1. doi: <https://doi.org/10.1016/B978-0-12-809731-1.00002-2>. URL <https://www.sciencedirect.com/science/article/pii/B9780128097311000022>.
- [12] (Thermochromic Liquid Crystals (TLCs) – thermochromatische Flüssigkristalle — tu-dresden.de. <https://tu-dresden.de/ing/maschinenwesen/ism/tfa/forschung/infrastruktur/messtechnik/thermochromic-liquid-crystals-tlcs-thermochromatische-fluessigkristalle>. [Accessed 17-Jul-2022].
- [13] Sylwia Kozłowska. Experimental Study on Transpiration Cooling Method through Additively Manufactured Porous Structures

- TU Delft Repositories. <http://resolver.tudelft.nl/uuid:65117bb9-2939-4810-a4ed-df59f32f663b>, 2021.
- [14] Michael Vollmer and Mollmann Klaus-Peter. *Infrared Thermal Imaging: Fundamentals, research and applications*, chapter Industrial Application: Detection of Gases. Wiley-VCH, 2010.
- [15] Crystran. Sapphire Optical Material — crystran.co.uk. <https://www.crystran.co.uk/optical-materials/sapphire-al2o3>.
- [16] NetScanner 9116 Pressure Scanner — te.com. <https://www.te.com/usa-en/product-CAT-SCS0002.html>.
- [17] 7220 16 channel measurement processor — Datascan Daq. <https://datascandaq.com/p/measurement-processors/7220-16-channel-measurement-processor/>.
- [18] Rosemount 2088 Gage and Absolute Pressure Transmitter — Emerson US — emerson.com. <https://www.emerson.com/en-us/catalog/rosemount-sku-2088-gage-and-absolute-pressure-transmitter>.
- [19] SITRANS FC MASS 2100 DI 3-15 — new.siemens.com. <https://new.siemens.com/us/en/products/automation/process-instrumentation/flow-measurement/coriolis/sitrans-f-c-mass-2100-di-3-15.html>.
- [20] Electrophysics® Introduces Titanium™ — irinfo.org. <https://irinfo.org/news-05-18-07/>.
- [21] V A Kurganov. HEAT TRANSFER COEFFICIENT. In *A-to-Z Guide to Thermodynamics, Heat and Mass Transfer, and Fluids Engineering*. Begell-house, 2011. doi: 10.1615/AtoZ.h.heat_transfer_coefficient.
- [22] Shailendra Naik. Basic aspects of gas turbine heat transfer. In *Heat Exchangers - Design, Experiment and Simulation*. InTech, April 2017.
- [23] Microturbines — WBDG - Whole Building Design Guide — wbdg.org. <https://www.wbdg.org/resources/microturbines>. [Accessed 27-Aug-2022].
- [24] A M Y Razak. Thermodynamics of gas turbine cycles. In *Industrial Gas Turbines*, pages 13–59. Elsevier, 2007.
- [25] E.R.G. Eckert and Jack B. Esgar. Survey of advantages and problems associated with transpiration cooling and film cooling of gas-turbine blades : Lewis Research Center, national advisory comitee for aeronautics. <https://archive.org/details/surveyofadvantag001ewi>, 1951. [Accessed Aug-2022].
- [26] C. M. Bell, H. Hamakawa, and P. M. Ligrani. Film Cooling From Shaped Holes . *Journal of Heat Transfer*, 122(2):224–232, 12 1999. ISSN 0022-1481. doi: 10.1115/1.521484. URL <https://doi.org/10.1115/1.521484>.

- [27] Ronald S. Bunker. A Review of Shaped Hole Turbine Film-Cooling Technology . *Journal of Heat Transfer*, 127(4):441–453, 03 2005. ISSN 0022-1481. doi: 10.1115/1.1860562. URL <https://doi.org/10.1115/1.1860562>.
- [28] Michael Gritsch, Will Colban, Heinz Schär, and Klaus Döbbeling. Effect of Hole Geometry on the Thermal Performance of Fan-Shaped Film Cooling Holes. *Journal of Turbomachinery*, 127(4):718–725, 04 2005. ISSN 0889-504X. doi: 10.1115/1.2019315. URL <https://doi.org/10.1115/1.2019315>.
- [29] *Experimental and Numerical Investigations of the NEKOMIMI Film Cooling Technology*, volume Volume 4: Heat Transfer, Parts A and B of *Turbo Expo: Power for Land, Sea, and Air*, 06 2012. doi: 10.1115/GT2012-68400. URL <https://doi.org/10.1115/GT2012-68400>.
- [30] Prasad Kalghatgi and Sumanta Acharya. Improved Film Cooling Effectiveness With a Round Film Cooling Hole Embedded in a Contoured Crater. *Journal of Turbomachinery*, 137(10), 06 2015. ISSN 0889-504X. doi: 10.1115/1.4030395. URL <https://doi.org/10.1115/1.4030395>. 101006.
- [31] Zheng Huang, Yin-Hai Zhu, Yan-bin Xiong, and Peixue Jiang. Investigation of supersonic transpiration cooling through sintered metal porous flat plates. *Journal of Porous Media*, 18, 01 2015. doi: 10.1615/JPorMedia.2015012159.
- [32] D. A. Nealy and S. B. Reider. Evaluation of Laminated Porous Wall Materials for Combustor Liner Cooling. *Journal of Engineering for Power*, 102(2): 268–276, 04 1980. ISSN 0022-0825. doi: 10.1115/1.3230247. URL <https://doi.org/10.1115/1.3230247>.
- [33] Gan Huang, Zheng Min, Li Yang, Pei-Xue Jiang, and Minking Chyu. Transpiration cooling for additive manufactured porous plates with partition walls. *International Journal of Heat and Mass Transfer*, 124:1076–1087, 2018. ISSN 0017-9310. doi: <https://doi.org/10.1016/j.ijheatmasstransfer.2018.03.110>. URL <https://www.sciencedirect.com/science/article/pii/S0017931017355126>.
- [34] Arne Tiddens, Kai Risthaus, Marc Röger, Hannes Stadler, and Bernhard Hoffschmidt. Induced infrared thermography: Flow visualizations under the extreme conditions of an open volumetric receiver of a solar tower. *International Journal of Heat and Fluid Flow*, 65:105–113, 2017. ISSN 0142-727X. doi: <https://doi.org/10.1016/j.ijheatfluidflow.2017.04.002>. URL <https://www.sciencedirect.com/science/article/pii/S0142727X16305872>.
- [35] Jonas Sandsten, Hans Edner, and Sune Svanberg. Gas imaging by infrared gas-correlation spectrometry. *Optics letters*, 21 23:1945–7, 1996.
- [36] Narayanan, Page, and Seyed-Yagoobi. Visualization of air flow using infrared thermography. *Experiments in Fluids*, 4:275–284, 2003.
- [37] Shane Transue, Sayed Mohsin Reza, Ann Halbower, and Min Choi. Behavioral analysis of turbulent exhale flows. In *IEEE Conference on Biomedical and Health Informatics 2018*, 04 2018. doi: 10.1109/BHI.2018.8333365.

- [38] Bourget, Liger-Belair, and Pron. Unraveling the release of gaseous co₂ during champagne serving through high-speed infrared imaging. *J Vis*, 16:47–52, 2013.
- [39] Howard Yoon, Meredith Brenner, Joseph Rice, Nathaniel Briggs, and Greg Gillen. Flow visualization of heated co₂ gas using thermal imaging - art. no. 62050u. volume 6205, pages U2050–U2050, 01 2006. ISBN 0-8194-6261-6. doi: 10.1117/12.664991.
- [40] Mark F. Reeder, Jim W. Crafton, Jordi Estevadeordal, Joseph DeLapp, Charles McNiel, Don Peltier, and Tina Reynolds. Clean seeding for flow visualization and velocimetry measurements. *Experiments in Fluids*, 48(5): 889–900, May 2010. ISSN 1432-1114. doi: 10.1007/s00348-009-0784-5. URL <https://doi.org/10.1007/s00348-009-0784-5>.
- [41] Gregory S. Manuel, Kamran Daryabeigi, David W. Alderfer, and Clifford J. Obara. In-flight off-surface flow visualization using infrared imaging. In *Nasa Langley Research Center*, 1991.
- [42] LCR Hallcrest. *Handbook of Thermochromic Liquid Crystal Technology*. Wiley-VCH.

Appendix

A Cost

In this section an estimate of the overall cost of the project will be computed. Equipment, human resources and materials needed for the completion of the project will be taken into account. Indirect costs such as managing, space used by the worker and equipment, use of electricity, ..., will be taken into account as a general cost.

All of the costs will be written in Swedish Krona (SEK), as was the currency used. The partial results will later be converted to Euro (EUR) for ease of reading.

After computing the different partial costs, a 33% increase will be added due to taxes and 20% due to general costs.

A.1 Partial Costs

Labour Costs

Labour costs are comprised by a Ph.D Engineer, as the supervisor of the project, and a MSc Engineer, as the worker. The associated net cost are 200 SEK / h and 140 SEK / h respectively.

| Category | SEK/h | h / week | Total Hours | Total Cost (SEK) | Total Cost (EUR) |
|---------------|-------|----------|-------------|------------------|------------------|
| Ph.D Engineer | 200 | 3 | 108 | 21600 | 2014.76 |
| MSc Engineer | 140 | 40 | 1440 | 201600 | 18804.44 |
| Total | | | | 223200 | 20819.2 |

Table 6.1: Labour Costs

Equipment

The operational cost of the equipment used during the extent of the internship are collected in Table 6.2. Regarding the test facility, only the cost of the measurement section of the test rig developed for this experiment has been accounted for as part of the test rig was already available from previous experiments.

The measuring equipment was already present in the lab. However, it has been taken into account as it could have been used for other projects.

All the costs have been adjusted to the length of the internship of 8 months.

| Name | Cost (SEK) | Operational Time (years) | Adjusted Cost (SEK) | (EUR) |
|-----------------------|------------|--------------------------|---------------------|---------|
| NetScanner Model 9116 | 30000 | 10 | 2000 | 186.55 |
| Rosemount 2088 | 20000 | 10 | 1333.33 | 124.37 |
| Datascan 7220 | 5000 | 10 | 333.33 | 31.09 |
| SITRANS FC MASS 2100 | 50000 | 10 | 3333.33 | 310.92 |
| Test Rig | 20000 | - | 20000 | 1865.52 |
| Work Computer | 20000 | 5 | 2666.67 | 248.74 |
| IR Window | 10000 | 10 | 666.67 | 62.18 |
| IR Camera | 1000000 | 20 | 33333.33 | 3109.2 |
| Total | | | 63666.66 | 5938.57 |

Table 6.2: Equipment Cost

Regarding the cost of the software, they are presented in Table 6.3. As in the equipment cost, it has been adjusted to the length of the internship of 8 months.

| Name | License Type | Cost (SEK) | Adjusted Cost (SEK) | (EUR) |
|------------|--------------|------------|---------------------|--------|
| Python | OpenSource | 0 | 0 | 0 |
| ResearchIR | 5 years | 30000 | 4000 | 373.1 |
| LabVIEW | 1 year | 5500 | 3666.67 | 342.01 |
| Total | | | 7666.67 | 715.11 |

Table 6.3: Software Cost

A.2 General Cost and Taxes

All the partial costs have been collected in Table 6.4. 33% of taxes and 10% regarding general costs have been added. In the case of the software and equipment, taxes have not been added as they were already included. General cost have been considered to account for indirect cost such as electricity, IT, calibration, etc.

| Description | Partial Cost (SEK) | Taxes (SEK) | General Cost (SEK) | Total Cost (SEK) | (EUR) |
|----------------|--------------------|-------------|--------------------|------------------|----------|
| Labor Cost | 223200 | 73656 | 44640 | 341496 | 31853.38 |
| Equipment Cost | 63666.66 | 0 | 12733.33 | 76399.99 | 7126.29 |
| Software Cost | 7666.67 | 0 | 1533.33 | 9200 | 858.14 |
| Total | | | | 427095.99 | 39837.81 |

Table 6.4: Total Cost

B Specifications

B.1 Measurement Equipment

NetScanner Model 9116

| Parameter | 9116 | Units | Comments |
|-----------------------------------|---------------------------------------|-------------------|---|
| Pressure Inputs | $\pm 1, \pm 2.5, \pm 5, \pm 15, +100$ | <i>psi</i> | Ranges above 100 <i>psi</i> are unidirectional only |
| Number of Pressure Inputs | 16 | | Available in any combination of ranges |
| Media | Dry | | non-corrosive gas |
| Proof Pressure | 3.0X 2.0X | FS min | range < 15 psi range 15-100 psi |
| Burst Pressure | 5.0X 3.0X | FS min | range < 15 psi range 15-100 psi |
| Max Line Pressure | 100 600 | psi | range < 5 psi range > 5 psi |
| Measurement Resolution | ± 0.003 | % FS | |
| Static Accuracy (After Rezero) | ± 0.05 ± 0.15 | %FS | range < 2.5 psi range > 2.5 psi |
| Total Thermal Error | ± 0.001 ± 0.0015 | %FS/ $^{\circ}$ C | range < 2.5 psi range > 2.5 psi |
| Line Pressure Effect | ± 0.001 ± 0.0008 | %FS/psi | range < 2.5 psi range > 2.5 psi |
| Measurement Rate | 500 | meas/ch/s | Engineering units |
| Calibrated Temperature Range | 0 to 60 | $^{\circ}$ C | |
| Operating Temperature Range | -20 to 70 | $^{\circ}$ C | |

Table 6.5: NetScanner Model 9116 Specifications [16]

Datascan 7220

| Parameter | Value |
|-------------------|---|
| Number of Inputs | 16 |
| Sensor Types | DC Voltage, Thermocouples, 4-20 mA |
| Resolution | 16 bits @ 40 Hz - 14 bits @ 400 Hz |
| Input Impedance | 300 $M\Omega$ |
| DC Voltage Ranges | 10V, 1.3V, 150mV, 20mV, Auto |
| Resolutions | 320 μ V, 40 μ V, 5 μ V, 0.625 μ V |
| Accuracy | $\pm 0.02\%$ reading + 0.01% range + 1 bit |

Table 6.6: Datascan 7220 Specifications [17]

Rosemount 2088

| Parameter | Value |
|-------------------|----------------------------------|
| Pressure range | -14.7 - 30 psi (-1.01 - 2.1 bar) |
| Protocol | 4-24 mA HART |
| Accuracy | 0.065% |
| Temperature Range | -20 to 80°C |

Table 6.7: Rosemount 2088 Specifications [18]

SITRANS FC MASS 2100

| Parameter | Value |
|------------------|-----------------------------|
| Measuring range | 0 - 5600 kg/h |
| Nominal Size | DI 3 to DI 15 (1/8" - 5/8") |
| Accuracy | $\leq 0.1\%$ of rate |
| Nominal Pressure | Max 410 bar |
| Sensor Design | One tube bended |
| Enclosure | IP65 (NEMA 4) |
| Approvals | ATEX EEx (ia) IIC T3-T6 |

Table 6.8: SITRANS FC MASS 2100 Specifications [19]

CEDIP Titanium 560M

| Parameter | Value |
|-------------------|------------------------------------|
| Detector Material | In Sb |
| Number of Pixels | 640 x 512 |
| Spectral Response | 3.6 - 5.1 μ m |
| Frame Rate | 100 Hz @ 640x512 - 4980 Hz @ 16x14 |
| Pitch | 15 x 15 μ m |
| Aperture | F/3 |

Table 6.9: CEDIP Titanium 560M Specifications [20]

B.2 Materials

IR Window

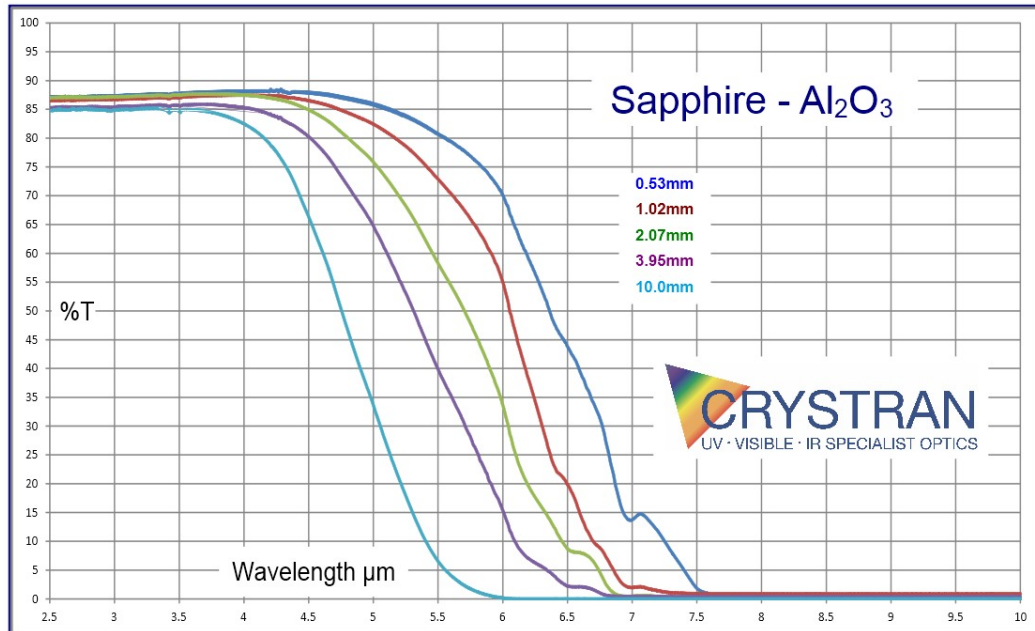


Figure 6.1: Transmittance IR Window Sapphire [15]

B.3 Hardware and Software

Hardware

Laptop HP zbook 15g3 (work computer)

- Processor: Intel Core i7-6820HQ with Intel HD graphics 530 (2.70 GHz, 2133 MHz, 8 MB L3 cache, 4 cores, 45W), up to 3.60 GHz with Intel Turbo Boost Technology
- Graphics Card: NVIDIA Quadro M1000M with 2 GB dedicated GDDR5 video memory Microsoft DirectX 12 (Shader Model 5.0) and OpenGL 4.4 capable
- RAM: 64 GB

Software

- Python: Post-processing of the results
- ResearchIR: Software for thermal analysis with IR cameras. Allows high speed data recording, real-time or playback analysis and reporting
- Labview: Used to collect and evaluate the data from all the different measurement devices.

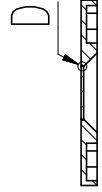
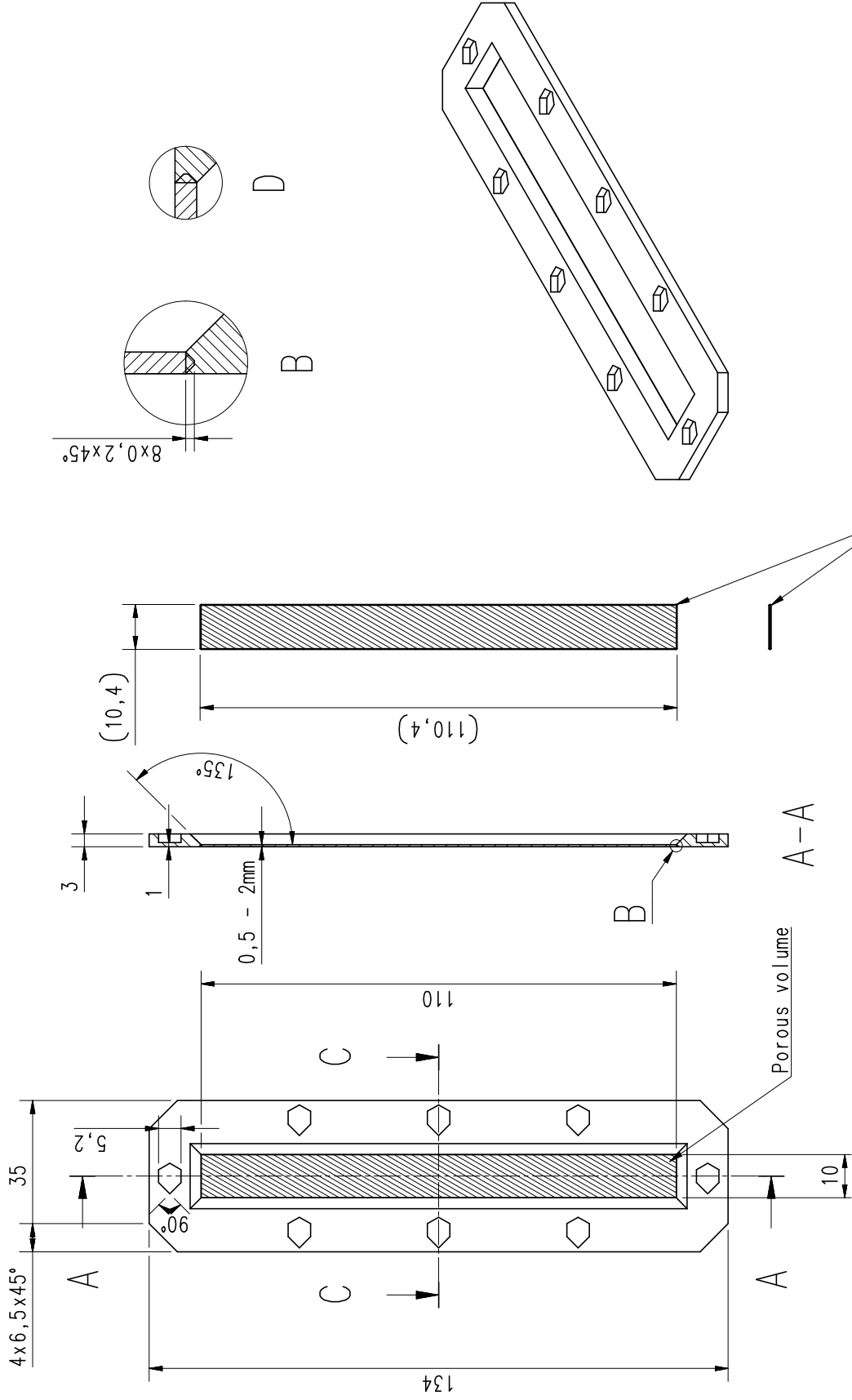
C Additional Information Test Objects

C.1 Chemical Composition Test Objects

| Element | Hastelloy-X | Inconel 625 |
|------------|--------------|-------------|
| Nickel | 47% | 58% (min) |
| Chromium | 22% | 20-23% |
| Molybdenum | 9% | 8 - 10% |
| Iron | 18% | 5% (max) |
| Niobium | 0.5% (max) | 3.15-4.15% |
| Tantalum | - | |
| Cobalt | 1.5% | 1% (max) |
| Silicon | 1% (max) | 0.5% (max) |
| Manganese | 1% (max) | 0.5% (max) |
| Titanium | 0.15% (max) | 0.4% (max) |
| Silver | - | 0.4% (max) |
| Carbon | 0.1% | 0.1% (max) |
| Sulphur | - | 0.01% (max) |
| Phosphorus | - | 0.01% (max) |
| Tungsten | 0.6% | - |
| Boron | 0.008% (max) | - |
| Aluminum | 0.5% (max) | - |

Table 6.10: Chemical composition of Hastelloy-X and Inconel 625

C.2 Technical Drawing Test Object



C-C

| FSP | Date | Name | Scale 1:1 | Based On |
|----------|------|------|-----------|----------|
| Created | | | Title | |
| Reviewed | | | | |
| Approved | | | | |
| 1st Appr | | | | |

Test piece
Porous test piece

| Ident-Number/Document-Number | Revision | Language | Sheet |
|------------------------------|----------|----------|-------|
| E1B100598463 | A | en | 1/1 |

Size
A3

D Additional Mathematical Derivations

D.1 CO_2 concentration and radiance absorption

$$A = \int_0^L \varepsilon c(z) dz \quad (6.1)$$

Beer's Law (Equation 6.1) relates the attenuation of light with its molar attenuation coefficient and molar concentration for non-scattering samples.

If c is uniform along the path¹, the equation simplifies to:

$$A = \varepsilon c L \quad (6.2)$$

The transmittance is defined as:

$$T = \frac{\text{surface radiation} - \text{absorbed radiation}}{\text{surface radiation}} = 10^{-A} \quad (6.3)$$

Combining Equation 6.2 and 6.3 and doing some reordering, we reach that, if the absorbed radiation is small with respect to the surface radiation:

$$c = \frac{-1}{\varepsilon L} \log \left(1 + \frac{-\text{absorbed radiation}}{\text{surface radiation}} \right) \approx \frac{1}{\varepsilon L \ln(10)} \frac{\text{absorbed radiation}}{\text{surface radiation}} \quad (6.4)$$

¹or its average value is taken